

# Constant Modulus Waveform Design with Interference Exploitation for DFRC Systems: A Block-Level Optimization Approach

Byunghyun Lee, *Graduate Student Member, IEEE*, Anindya Bijoy Das, *Member, IEEE*, David J. Love, *Fellow, IEEE*, Christopher G. Brinton, *Senior Member, IEEE* and James V. Krogmeier, *Senior Member, IEEE*

**Abstract**—Dual-function radar-communication (DFRC) is a key enabler of location-based services for next-generation communication systems. In this paper, we investigate the problem of designing constant modulus waveforms for DFRC systems. For high-precision radar sensing, we consider joint optimization of the correlation properties and spatial beam pattern. For communication, we employ constructive interference-based block-level precoding (CI-BLP) to leverage distortion induced by multiuser multiple-input multiple-output (MU-MIMO) and radar transmission on a block level. We propose two solution algorithms based on the alternating direction method of multipliers (ADMM) and majorization-minimization (MM) principles, which are effective for small and large block sizes, respectively. The proposed ADMM-based solution decomposes the nonconvex formulated problem into multiple tractable subproblems, each of which admits a closed-form solution. To accelerate convergence of the MM-based solution, we propose an improved majorizing function that leverages a novel diagonal matrix structure. After majorization, we decompose the approximated problem into independent subproblems for parallelization, mitigating the complexity that increases with block size. We then evaluate the performance of the proposed algorithms through a series of numerical experiments. Simulation results demonstrate that the proposed methods can substantially enhance spatial/temporal sidelobe suppression through block-level optimization.

**Index Terms**—Integrated sensing and communication (ISAC), dual-function radar-communication (DFRC), interference exploitation, multiple-input multiple-output (MIMO)

## I. INTRODUCTION

In the upcoming 6G era, communication networks are expected to offer not only connectivity but also sensing capabilities, enabled by integrated sensing and communications (ISAC) technology [1]. In line with this, standardization bodies such as the Third Generation Partnership Project (3GPP) and European Telecommunication Standard Institution (ETSI) have initiated investigations of ISAC to support location-based services such as vehicular communications, intelligent factories, and electromagnetic exposure reduction [2]–[4]. Early works in ISAC have proposed embedding information within radar pulses and radar-communication coexistence [5].

A preliminary version of this work has been accepted for publication in the International Conference on Communications (ICC), 2024.

This work is supported in part by the National Science Foundation under grants EEC-1941529, CNS-2212565, and CNS-2225578 and the Office of Naval Research under grant N000142112472.

Byunghyun Lee, Anindya Bijoy Das, David J. Love, Christopher G. Brinton, and James V. Krogmeier are with the Elmore Family School of Electrical and Computer Engineering, Purdue University, West Lafayette, IN 47907 USA (Email: {lee4093, das207, djlove, cgb, jvk}@purdue.edu).

In turn, dual-function radar-communication (DFRC), which shares both spectrum and hardware, has attracted significant research interest due to its potential to improve spectral, cost, and energy efficiency [6]–[10]. In this paper, we address the problem of designing waveforms for DFRC systems. In the rest of this section, we discuss our design principles and related works, and summarize our contributions.

### A. Our Design Principles and Related Work

**Constant Modulus Waveform Design:** In DFRC systems, high-power transmissions are often employed to enable precise and robust radar sensing. Under high-power conditions, a high peak-to-average power ratio (PAPR) may cause distorted signal outputs at high-power amplifiers (HPAs) [11], [12]. Therefore, it is crucial to design constant modulus waveforms to maintain the efficiency of HPAs and prevent such distortion. Some past DFRC works have investigated the problem of designing constant modulus waveforms [6], [13]–[15]. The work in [6] minimized multi-user interference under constant modulus and radar waveform similarity constraints. In [13], radar signal-to-noise ratio (SNR) was maximized under constant modulus and per-user interference constraints. As an alternative approach, [15], [16] considered a PAPR constraint to circumvent the problem of nonlinearity in HPAs.

**Interference Exploitation:** In the DFRC context, the design of constant modulus waveforms requires incorporating explicit data symbol information, which is closely related to symbol-level precoding (SLP) [17], [18]. Unlike traditional precoding schemes that only use channel information, SLP leverages both channel and data symbol information to exploit constructive interference (CI), which enhances communication signal power. Despite extensive research on CI-based SLP (CI-SLP), the use of CI-SLP for DFRC systems has been relatively limited. In [14], a beam pattern design problem was tackled under per-user CI and constant modulus constraints. This work focused on symbol-by-symbol optimization, which requires solving an optimization problem at every symbol time. To mitigate the computational burden, [19] studied block-level interference exploitation, also referred to as CI-based block-level precoding (CI-BLP), which synthesizes a transmission block directly or a precoder that is constant within a frame/block. The block-level waveform optimization for DFRC systems was initially investigated in [15], which employed space-time adaptive processing (STAP) that incorporates known target and clutter information into the waveform design. However, target

and clutter information may not always be available, which motivates an alternative approach that does not rely on such information.

**Correlation Property Optimization:** From a radar viewpoint, block-level waveform design incorporates the temporal aspects of the waveform. Addressing waveform correlation properties is pivotal for high-resolution radar sensing, as it directly impacts the quality of range estimation. In previous works, imposing a similarity constraint has been a prevalent approach to address this challenge [6], [15], [16], [20], [21]. This ensures that the designed waveform retains the space-time correlation properties of a reference waveform, such as linear frequency modulated (LFM) waveforms. Nonetheless, this approach offers an indirect solution to space-time sidelobes and thus lacks direct control over them. To overcome the limitations of imposing the similarity constraint, alternative approaches have optimized explicit sidelobe cost functions such as integrated sidelobe level (ISL) and peak sidelobe level (PSL) [22]–[26]. Most works have focused on suppressing spatial and temporal sidelobes individually. Yet, space-time correlation properties need to be addressed collectively to separate targets at different points in space and time [27], [28].

In this paper, we address the problem of designing constant modulus waveforms for DFRC systems. Our approach directly designs the transmit space-time matrix rather than designing a linear precoding matrix. We employ CI-BLP to take advantage of CI on a block level without the need for symbol-by-symbol optimization. Unlike prior works on CI-BLP that aim to reduce complexity [19] or signaling overhead [29], we focus on the joint design of the spatial and temporal properties of the waveform to achieve high-resolution radar sensing. To this end, we formulate the problem as a joint optimization of beam pattern and space-time correlations subject to the CI constraints. To tackle the formulated optimization problem, we propose two algorithms based on the alternating direction method of multipliers (ADMM) and majorization-minimization (MM) techniques.

### B. Summary of Contributions

Our contributions can be summarized as follows.

- We formulate a constant modulus waveform design problem for DFRC systems. In particular, we consider joint optimization of the spatial beam pattern and space-time sidelobes for high sensing resolution. For communication, we employ CI-BLP to lower the symbol error rate by leveraging CI in the presence of multiuser and radar transmission. We prove that the formulated problem is a non-convex NP-hard problem.
- Next, we propose an ADMM-based algorithm, where using the variable splitting technique, we break down the formulated problem into multiple tractable subproblems. We derive a closed-form solution to each of the subproblems, which enables alternating updates of variables.
- We develop an additional solution based on the MM method and the method of Lagrange multipliers, which offers a parallelization capability. We propose a novel diagonal matrix structure that enables tight majorization for quadratic functions to accelerate convergence.

- We analyze the computational complexity of the proposed algorithms and demonstrate that the proposed ADMM algorithm is more efficient for small block sizes while the MM algorithm is suitable for large block sizes.
- Finally, we conduct a series of numerical simulations to evaluate the proposed algorithms, and verify their effectiveness in comparison to the existing method [14].

The rest of the paper is organized as follows. In Sec. II, we provide the system model including the radar and communication models, and formalize our waveform design problem. Then, in Sec. III and Sec. IV, we develop our MM-based and ADMM-based solutions, respectively. Next, in Sec. V, we provide the complexity analyses of the proposed solutions. In Sec. VI, we evaluate the performances of our proposed algorithms in comparison with the baseline algorithm, and finally, we conclude the paper in Sec. VII.

**Notation:** Vectors and matrices are denoted by boldface lowercase and uppercase letters, respectively.  $(\cdot)^T$ ,  $(\cdot)^*$ ,  $(\cdot)^H$ , and  $(\cdot)^{-1}$  are the transpose, conjugate, conjugate transpose, and inverse operators, respectively.  $|\cdot|$  and  $\|\cdot\|$  denotes the absolute and 2-norm operators, respectively.  $\text{diag}(\cdot)$  is the diagonal matrix, with diagonal entries consisting of the input vector.  $\text{vec}(\cdot)$  is the vectorization of a matrix, while  $\text{mat}(\cdot)$  reshapes a vector into a matrix.  $\text{Tr}(\cdot)$  is the trace of a matrix.  $\mathbb{E}[\cdot]$  is the expectation operator.  $Q_{i,j}$  denotes the  $(i,j)$ th entry of a matrix  $\mathbf{Q}$ .  $\mathbf{0}$ ,  $\mathbf{1}$ , and  $\mathbf{I}$  represent the all-zeros, all-ones, and identity matrices, respectively.  $\angle$  is the phase of a complex number.  $\otimes$  denotes the Kronecker product.  $\nabla$  denotes the gradient operation.  $[\mathbf{x}, \mathbf{y}]^{(i)}$  denotes  $[\mathbf{x}^{(i)}, \mathbf{y}^{(i)}]$ .

## II. SYSTEM MODEL AND PROBLEM FORMULATION

### A. System Setup

Consider a downlink narrowband DFRC system where a base station (BS) operates as a multi-user MIMO (MU-MIMO) transmitter and collocated MIMO radar simultaneously, as depicted in Fig. 1. The BS is equipped with transmit and receive arrays of  $N_T$  and  $N_R$  antennas, respectively. Without loss of generality, we consider the uniform linear array (ULA) for both the transmit and receive arrays. The primary function of the considered system is radar sensing, while the secondary function is communication. To accomplish the dual functions of radar and communication, this paper focuses on downlink transmission, where the BS transmits a discrete-time waveform matrix  $\mathbf{X} \in \mathbb{C}^{N_T \times L}$  in each transmission block. The waveform matrix  $\mathbf{X}$  can be seen as a train of subpulses containing communication information. The  $(n, \ell)$ th entry  $X_{n,\ell}$  of  $\mathbf{X}$  represents the  $\ell$ th radar subpulse and  $\ell$ th discrete-time transmit symbol of  $L$  total for the  $n$ th transmit antenna.

### B. Radar Model

Consider  $Q$  far-field point targets at azimuth angles  $\theta_1, \dots, \theta_Q$  and range bins  $\tau_1, \dots, \tau_Q$ . To detect the targets, the BS collects reflected signals using the receive antennas. The received echo signal at the BS is given by [30], [31]

$$\mathbf{Z} = \sum_{q=1}^Q \kappa_q \mathbf{b}(\theta_q) \mathbf{a}^H(\theta_q) \mathbf{X} \mathbf{J}_{\tau_q - \tau_1} + \mathbf{W}, \quad (1)$$

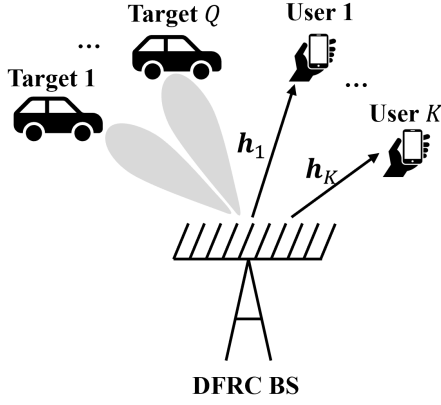


Figure 1: Illustration of a DFRC system. The BS transmits a dual-functional waveform in the downlink to search  $Q$  target directions and serve  $K$  communication users simultaneously.

where  $\kappa_q \in \mathbb{C}$  is the complex amplitude proportional to the radar cross-section (RCS) of target  $q$ ,  $\mathbf{a}(\cdot) \in \mathbb{C}^{N_T}$  is the steering vector of the transmit array,  $\mathbf{b}(\cdot) \in \mathbb{C}^{N_R}$  is the steering vector of the receive arrays,  $\mathbf{J}_{\tau q - \tau_1} \in \mathbb{R}^{L \times L}$  is the shift matrix for target  $q$ , and  $\mathbf{W} \in \mathbb{C}^{N_R \times L}$  is independent and identically distributed (i.i.d.) noise drawn from  $\mathcal{CN}(0, \sigma_r^2)$ . The shift matrix accounts for the round-trip delay between the BS and a target, which is given by [32]

$$[\mathbf{J}_\tau]_{i,j} = \begin{cases} 1, & \text{if } j - i = \tau \\ 0, & \text{otherwise.} \end{cases} \quad (2)$$

where  $\tau$  is the time shift.

### 1) Beam Pattern Shaping Cost

In radar waveform design, it is essential to maximize the mainlobe power directed toward targets while minimizing sidelobes. This strategy ensures strong return signals from the targets and suppresses undesired signals caused by clutter. Given the waveform  $\mathbf{X}$ , the beam pattern at angle  $\theta$  is given by  $G(\mathbf{X}, \theta) = \|\mathbf{a}^H(\theta)\mathbf{X}\|^2 = \mathbf{a}^H(\theta)\mathbf{X}\mathbf{X}^H\mathbf{a}(\theta)$  where  $\mathbf{a}(\theta) \in \mathbb{C}^{N_T}$  is the steering vector of the transmit array [33]. The beam pattern can be expressed in vector form as  $\tilde{G}(\mathbf{x}, \theta) = \|(\mathbf{I}_L \otimes \mathbf{a}^H(\theta))\mathbf{x}\|^2 = \mathbf{x}^H\mathbf{A}_u\mathbf{x}$  where  $\mathbf{A}_u = (\mathbf{I}_L \otimes \mathbf{a}^H(\theta))^H(\mathbf{I}_L \otimes \mathbf{a}^H(\theta))$  and  $\mathbf{x} = \text{vec}(\mathbf{X})$ . To obtain the desired properties, we minimize the mean square error (MSE) between the ideal beam pattern and the actual beam pattern, which can be expressed as

$$g_{bp}(\alpha, \mathbf{x}) = \sum_{u=1}^U |\alpha G_d(\theta_u) - \tilde{G}(\mathbf{x}, \theta_u)|^2, \quad (3)$$

where  $U$  is the number of angle bins,  $\alpha$  is the scaling coefficient, and  $G_d(\theta_u)$  is the desired beam pattern at angle  $\theta_u$ . Here, we have approximated the beam pattern MSE with a finite number  $U$  of angle bins. The scaling coefficient  $\alpha$  adjusts the amplitude of the beam pattern that varies according to the BS transmit power. Given the available closed-form solution to  $\alpha$ , the beam pattern shaping cost can be expressed in compact vector form as [14], [34]

$$\tilde{g}_{bp}(\mathbf{x}) = \sum_{u=1}^U |\mathbf{x}^H \mathbf{B}_u \mathbf{x}|^2, \quad (4)$$

where  $\mathbf{B}_u \triangleq G_d(\theta_u) \sum_{u'=1}^U \mathbf{A}_{u'} G_d(\theta_{u'}) \left( \sum_{u'=1}^U G_d^2(\theta_{u'}) \right)^{-1} - \mathbf{A}_u$ .

### 2) Space-time Autocorrelation and Cross-Correlation Integrated Sidelobe Levels (ISLs)

Since the ambiguity of a radar waveform has a significant impact on parameter estimation quality [27], [28], it is critical to address its ambiguity characteristics. We consider the space-time correlation function to quantify such ambiguity in the radar waveform. The space-time correlation function is defined as the correlation between a radar waveform and its echo reflected from different angle and range bins [35], [36], which is given by  $\chi_{\tau, q, q'}(\mathbf{X}) = |\mathbf{a}^H(\theta_q)\mathbf{J}_\tau \mathbf{X} \mathbf{a}^H(\theta_{q'})|^2$ , where  $\mathbf{J}_\tau \in \mathbb{R}^{L \times L}$  is the shift matrix [32]. The space-time correlation function can be rewritten in vector form as [34]  $\chi_{\tau, q, q'}(\mathbf{x}) = |\mathbf{x}^H \mathbf{D}_{\tau, q, q'} \mathbf{x}|^2$ , where  $\mathbf{D}_{\tau, q, q'} = \mathbf{J}_{-\tau} \otimes \mathbf{a}(\theta_{q'}) \mathbf{a}^H(\theta_q)$ . For a given parameter set  $(\tau, q, q')$ , the space-time correlation function  $\chi_{\tau, q, q'}(\mathbf{x})$  describes the correlation between angles  $\theta_q$  and  $\theta_{q'}$  at a range bin  $\tau$ . When  $q = q'$ , the space-time correlation function represents the autocorrelation properties at angle  $\theta_q$ . Then, the autocorrelation integrated sidelobe level (ISL) can be obtained as

$$g_{ac}(\mathbf{x}) = \sum_{q=1}^Q \sum_{\substack{\tau=-P+1 \\ \tau \neq 0}}^{P-1} \chi_{\tau, q, q}(\mathbf{x}), \quad (5)$$

where  $Q$  is the number of target directions of interest and  $P$  is the largest range bin of interest with  $P-1 \leq L$ . On the other hand, when  $q \neq q'$ , the space-time correlation function  $\chi_{\tau, q, q'}$  represents the cross-correlation properties between angles  $\theta_q$  and  $\theta_{q'}$  at a range bin  $\tau$ . The cross-correlation ISL is given by

$$g_{cc}(\mathbf{x}) = \sum_{q=1}^Q \sum_{\substack{q'=1 \\ q' \neq q}}^Q \sum_{\tau=-P+1}^{P-1} \chi_{\tau, q, q'}(\mathbf{x}). \quad (6)$$

By minimizing the defined ISL costs, we aim to enhance sensing resolution in space and time.

### C. Communication Model and QoS Constraint

Consider MU-MIMO transmission where the BS serves  $K$  single antenna users simultaneously, i.e.,  $N_T \geq K$ . We adopt a block-fading channel model where the communication channels remain the same within a transmission block. The  $\ell$ th received symbol at user  $k$  can be written as

$$y_{\ell, k} = \mathbf{h}_k^H \mathbf{x}_\ell + n_{\ell, k}, \quad (7)$$

where  $\mathbf{x}_\ell$  is the  $\ell$ th column of  $\mathbf{X}$  containing the  $\ell$ th communication symbol and  $\ell$ th radar subpulse,  $\mathbf{h}_k \in \mathbb{C}^{N_T}$  is the channel from the BS to user  $k$ , and  $n_{\ell, k} \in \mathbb{C}$  is Gaussian noise with  $n_{\ell, k} \sim \mathcal{CN}(0, \sigma^2)$ . We assume the BS has perfect knowledge of the user channels  $\mathbf{h}_k \in \mathbb{C}^{N_T}$  for  $k = 1, \dots, K$ . The codeword for user  $k$  is given by  $\mathbf{s}_k = [s_{1,k}, \dots, s_{L,k}]^T \in \mathbb{C}^L$  where each symbol  $s_{\ell, k}$  is drawn from a constellation  $\mathcal{S}$ . As discussed earlier, the CI-based approaches utilize both channel and symbol information for designing waveforms. In what follows, we detail the relationship between the desired codeword  $\mathbf{s}_k$  and the transmit signal  $\mathbf{X}$ .

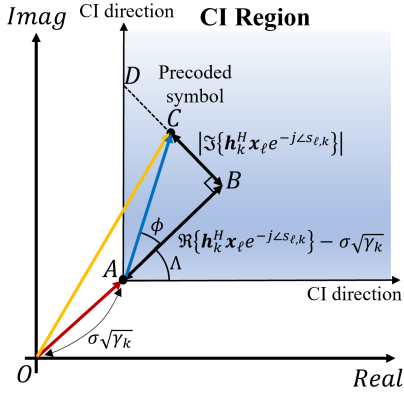


Figure 2: Constructive interference (CI) region. The  $\ell$ th noiseless received symbol  $\mathbf{h}_k^H \mathbf{x}_\ell$  for user  $k$  lies within the CI region if the inequality  $|\overline{BD}| \geq |\overline{BC}|$  holds.

#### Per-User Communication QoS Constraint

To ensure a baseline quality of service (QoS) for the communication users, we consider a CI-BLP approach to exploit the distortion induced by MU-MIMO and radar transmission. CI refers to an unintended signal that moves the precoded symbol farther away from its corresponding decision boundaries in the constructive direction. Unlike conventional precoding that eliminates distortion, the CI-BLP approach aims to locate the received symbols within the CI region, thereby reducing the symbol error rate.

This paper focuses on the  $M$ -phase shift keying<sup>1</sup> (M-PSK) constellation, where  $M = 4$ , i.e., quadrature-PSK (QPSK). Fig. 2 describes the condition under which the precoded symbol lies within the CI region.  $\overline{OC} = \mathbf{h}_k^H \mathbf{x}_\ell$  denotes the  $\ell$ th noise-free precoded symbol for user  $k$ .  $\overline{OA} = p \cdot s_{\ell,k}$  is the  $\ell$ th scaled data symbol for user  $k$ , where  $p = \sigma\sqrt{\gamma_k}$  and  $\gamma_k$  is the SNR target.  $\overline{OC}$  falls into the CI region if the distortion  $\overline{AC}$  is in the constructive direction. From the geometry, the CI condition can be expressed as  $\Lambda \geq \phi$  where  $\phi$  is the angle between  $\overline{AB}$  and  $\overline{AC}$ , and  $\Lambda = \pi/M$ , which is equivalent to  $|\overline{BD}| \geq |\overline{BC}|$ . The length  $|\overline{BC}|$  can be expressed as  $|\overline{BC}| = |\Im\{\mathbf{h}_k^H \mathbf{x}_\ell e^{-j\angle s_{\ell,k}}\}|$ , while the length  $|\overline{BD}|$  can be expressed as  $|\overline{BD}| = |\overline{AB}| \tan \Lambda = \Re\{\mathbf{h}_k^H \mathbf{x}_\ell e^{-j\angle s_{\ell,k}} - \sigma\sqrt{\gamma_k}\} \tan \Lambda$ .

Combining the above results, the communication constraint for  $\ell$ th symbol of user  $k$  can be formulated as [37]

$$\Re\{\mathbf{h}_k^H \mathbf{x}_\ell e^{-j\angle s_{\ell,k}} - \sigma\sqrt{\gamma_k}\} \tan \Lambda - |\Im\{\mathbf{h}_k^H \mathbf{x}_\ell e^{-j\angle s_{\ell,k}}\}| \geq 0.$$

The above CI constraint can be transformed into [14]

$$\Re\{\hat{\mathbf{h}}_{\ell,m}^H \mathbf{x}_\ell\} \geq \Gamma_m, \quad \forall \ell = 1, 2, \dots, L, \quad \forall m = 1, 2, \dots, 2K, \quad (8)$$

where

$$\begin{aligned} \hat{\mathbf{h}}_{\ell,2k}^H &\triangleq \mathbf{h}_k^H e^{-j\angle s_{\ell,k}} (\sin \Lambda - j \cos \Lambda), \\ \hat{\mathbf{h}}_{\ell,2k-1}^H &\triangleq \mathbf{h}_k^H e^{-j\angle s_{\ell,k}} (\sin \Lambda + j \cos \Lambda), \quad \text{and} \\ \Gamma_{2k} &\triangleq \sigma\sqrt{\gamma_k} \sin \Lambda, \quad \Gamma_{2k-1} \triangleq \sigma\sqrt{\gamma_k} \sin \Lambda. \end{aligned}$$

Due to the limited space, we refer the readers to [14], [37] for a detailed derivation. With this, the CI constraint can be

<sup>1</sup>Although the main focus of this paper is the PSK scenario, it is possible to extend it to quadrature amplitude modulation (QAM), as shown in [19].

reformulated with respect to vector  $\mathbf{x}$  as  $\Re\{\tilde{\mathbf{h}}_{\ell,m}^H \mathbf{x}\} \geq \Gamma_m$ , where  $\tilde{\mathbf{h}}_{\ell,m}^H \triangleq \mathbf{e}_{\ell,L}^T \otimes \hat{\mathbf{h}}_{\ell,m}^H$  and  $\mathbf{e}_{\ell,L}^T$  denotes the  $\ell$ th column of the  $L \times L$  identity matrix.

#### D. Constant Modulus Constraint

In order to maximize the efficiency of HPAs, it is essential to design a constant envelope waveform of the BS. Hence, we impose a constant modulus constraint to ensure the entries of the waveform have a constant amplitude, which can be expressed as  $|x_n| = \sqrt{P_T/N_T}$ ,  $\forall n$ , where  $P_T$  is the transmit power and  $x_n$  is the  $n$ th entry of  $\mathbf{x}$ . The feasible set of the constant modulus constraint is a complex circle manifold [38], which can be expressed as  $\mathcal{M} = \{\mathbf{x} \in \mathbb{C}^{LN_T} : |x_n| = \sqrt{P_T/N_T} \forall n\}$ .

#### E. Problem Formulation

Our objective is to design a dual-functional waveform that detects the targets of interest while serving the communication users simultaneously. To this end, we minimize the beam pattern shaping cost, to maximize the mainlobe power aimed toward targets  $\theta_1, \theta_2, \dots, \theta_Q$  while minimizing spatial sidelobes. Furthermore, we minimize the space-time ISL to reduce the autocorrelations of each target and the cross-correlations among the targets. For communication, we impose the CI constraint to ensure that the communication symbols exist within the CI region, thereby meeting the QoS requirement. By taking these design goals into account, the waveform design problem is formulated as

$$\begin{aligned} \min_{\mathbf{x}} \quad & \omega_{bp} \tilde{g}_{bp}(\mathbf{x}) + \omega_{ac} g_{ac}(\mathbf{x}) + \omega_{cc} g_{cc}(\mathbf{x}) \\ \text{s.t.} \quad & \mathbf{C1} : \Re\{\tilde{\mathbf{h}}_{\ell,m}^H \mathbf{x}\} \geq \Gamma_m, \quad \forall \ell, m \\ & \mathbf{C2} : |x_n| = \sqrt{\frac{P_T}{N_T}}, \quad \forall n = 1, 2, \dots, LN_T \end{aligned} \quad (9)$$

where  $\omega_{bp}, \omega_{ac}, \omega_{cc} \geq 0$  are the weights for the beam pattern shaping cost (4), autocorrelation ISL (5) and cross-correlation ISL (6), respectively. **C1** is the communication QoS constraint, and **C2** is the constant modulus constraint. By normalizing the constant modulus constraint, we can reformulate the above problem as

$$\begin{aligned} \min_{\mathbf{x}} \quad & \omega_{bp} \tilde{g}_{bp}(\mathbf{x}) + \omega_{ac} g_{ac}(\mathbf{x}) + \omega_{cc} g_{cc}(\mathbf{x}) \\ \text{s.t.} \quad & \mathbf{C1} : \Re\{\tilde{\mathbf{h}}_{\ell,m}^H \mathbf{x}\} \geq \tilde{\Gamma}_m, \quad \forall \ell, m \\ & \mathbf{C2} : |x_n| = 1, \quad \forall n = 1, 2, \dots, LN_T \end{aligned} \quad (10)$$

where  $\tilde{\Gamma}_m = \sqrt{\frac{N_T}{P}} \Gamma_m$ . We have the following theorem:

**Theorem 1.** Problem (10) is nonconvex.

See Appendix A for detailed proof.

The formulated problem is intractable due to the nonconvex fourth-order objective and constant modulus constraint. To tackle this, we develop solutions based on ADMM and MM techniques. Briefly speaking, the ADMM algorithm reduces the order of the objective and decomposes the constraints using the variable splitting technique. The MM algorithm approximates the objective with a lower-order function and applies the method of Lagrange multipliers to manage the constant modulus constraint. The ADMM-based approach is

particularly efficient for low  $L$  due to its iterations with closed-form solutions, while the MM-based approach is preferable for high  $L$  owing to its parallelization capability. We detail the proposed algorithms in the subsequent sections.

**Remark 1.** The approach in [14] solved a beam pattern optimization problem with CI and constant modulus constraints. This work focused on symbol-by-symbol optimization by designing vectors  $\mathbf{x}_1, \mathbf{x}_2, \dots, \mathbf{x}_L$  separately to transmit a codeword of length  $L$ . Moreover, the temporal aspects of the waveform were not considered, which are crucial for sensing resolution. To tackle this challenge, we employ per-block optimization that directly designs a transmit matrix  $\mathbf{X}$ , which is equivalent to using a constant precoder within a transmission block [39]. Furthermore, we jointly optimize the waveform space and time properties for high sensing resolution.

Note that the term ‘‘block-level’’ indicates that waveform optimization occurs on a per-block basis, rather than on a per-symbol basis [39]. The CI-BLP approach differs from traditional linear block-level precoding as it still involves per-symbol CI constraints [19], [29]. Despite this, the CI-BLP approach takes advantage of block-level optimization, including complexity reduction, block-level power allocation [19], and signaling overhead reduction [29]. This paper focuses on the DFRC aspects of the CI-BLP approach by jointly optimizing spatial and temporal waveform properties.

### III. ADMM-BASED ALGORITHM

In this section, we develop an ADMM-based solution for addressing the non-convexity of the problem (10). ADMM techniques aim to combine the decomposability of the dual ascent method and the desirable convergence properties of the method of Lagrange multipliers [40]. The key advantage of ADMM is that it can decompose an intractable problem into multiple tractable subproblems that involve closed-form solutions. To this end, most existing ADMM-based algorithms focus on breaking down the objective into multiple independent parts for alternating updates. In contrast, [41] proposed a unique approach where an ADMM algorithm was employed to reduce the order of a quartic objective function and decompose the constant modulus constraint. Inspired by this approach, we adopt an ADMM technique to handle the fourth-order objective and constant modulus constraint. In what follows, we elaborate on the process of decomposing the problem (10) into smaller subproblems and their solutions.

#### A. ADMM Formulation

First, we reformulate the problem in (10) by introducing auxiliary variables  $\mathbf{u} \in \mathbb{C}^{LN_T}$ ,  $\mathbf{v} \in \mathbb{C}^{LN_T}$ , and  $z_{\ell,m} \in \mathbb{C}$  for  $\ell = 1, 2, \dots, L$  and  $m = 1, 2, \dots, 2K$  as

$$\begin{aligned} \min_{\mathbf{x}, \mathbf{u}, \mathbf{v}, \{z_{\ell}\}_{\ell=1}^L} & \omega_{bp} \tilde{g}_{bp}(\mathbf{x}, \mathbf{v}) + \omega_{ac} g_{ac}(\mathbf{x}, \mathbf{v}) + \omega_{cc} g_{cc}(\mathbf{x}, \mathbf{v}) \\ \text{s.t.} & \Re\{z_{\ell,m}\} \geq \tilde{\Gamma}_m, \forall \ell, m \\ & \mathbf{x} = \mathbf{v}, \quad \mathbf{u} = \mathbf{v}, \\ & z_{\ell,m} = \tilde{\mathbf{h}}_{\ell,m}^H \mathbf{x}, \forall \ell, m \end{aligned} \quad (11)$$

where  $\mathbf{z}_{\ell} = [z_{\ell,1}, z_{\ell,2}, \dots, z_{\ell,2K}]$ ,

$$\begin{aligned} \tilde{g}_{bp}(\mathbf{x}, \mathbf{v}) & \triangleq \sum_{u=1}^U |\mathbf{x}^H \mathbf{B}_u \mathbf{v}|^2, \\ g_{ac}(\mathbf{x}, \mathbf{v}) & \triangleq \sum_{q=1}^Q \sum_{\substack{\tau=-P+1, \\ \tau \neq 0}}^{P-1} |\mathbf{x}^H \mathbf{D}_{\tau,q} \mathbf{v}|^2, \text{ and} \\ g_{cc}(\mathbf{x}, \mathbf{v}) & \triangleq \sum_{q=1}^{Q-1} \sum_{\substack{q'=1, \tau=-P+1 \\ q' \neq q}}^Q \sum_{\tau=-P+1}^{P-1} |\mathbf{x}^H \mathbf{D}_{\tau,q,q'} \mathbf{v}|^2. \end{aligned} \quad (12)$$

By substituting one  $\mathbf{x}$  with an auxiliary variable  $\mathbf{v}$ , the objective is bi-convex, i.e., convex in  $\mathbf{x}$  with  $\mathbf{v}$  fixed and in  $\mathbf{v}$  with  $\mathbf{x}$  fixed [41]. Moreover, the constant modulus and QoS constraints are decoupled through the introduced auxiliary variables  $\mathbf{u}$  and  $\{z_{\ell}\}_{\ell=1}^L$ . In consequence, the reformulated problem becomes an unconstrained problem with respect to variables  $\mathbf{x}$  and  $\mathbf{v}$ . With fixed  $\mathbf{v}$ , the objective function can be rewritten in quadratic form with respect to  $\mathbf{x}$  as

$$g(\mathbf{x}) = \omega_{bp} \mathbf{x}^H \mathbf{G}_1 \mathbf{x} + \omega_{ac} \mathbf{x}^H \mathbf{G}_2 \mathbf{x} + \omega_{cc} \mathbf{x}^H \mathbf{G}_3 \mathbf{x}, \quad (13)$$

where

$$\begin{aligned} \mathbf{G}_1 & \triangleq \sum_{u=1}^U \mathbf{B}_u \mathbf{v} \mathbf{v}^H \mathbf{B}_u^H, \quad \mathbf{G}_2 \triangleq \sum_{q=1}^Q \sum_{\substack{\tau=-P+1, \\ \tau \neq 0}}^{P-1} \mathbf{D}_{\tau,q,q} \mathbf{v} \mathbf{v}^H \mathbf{D}_{\tau,q,q}^H, \\ \mathbf{G}_3 & \triangleq \sum_{q=1}^{Q-1} \sum_{\substack{q'=1, \tau=-P+1 \\ q' \neq q}}^Q \sum_{\tau=-P+1}^{P-1} \mathbf{D}_{\tau,q,q'} \mathbf{v} \mathbf{v}^H \mathbf{D}_{\tau,q,q'}^H. \end{aligned}$$

Similarly, the objective function can be rewritten in quadratic form with respect to  $\mathbf{v}$  as

$$\tilde{g}(\mathbf{v}) = \omega_{bp} \mathbf{v}^H \mathbf{T}_1 \mathbf{v} + \omega_{ac} \mathbf{v}^H \mathbf{T}_2 \mathbf{v} + \omega_{cc} \mathbf{v}^H \mathbf{T}_3 \mathbf{v}, \quad (14)$$

where

$$\begin{aligned} \mathbf{T}_1 & \triangleq \sum_{u=1}^U \mathbf{B}_u^H \mathbf{x} \mathbf{x}^H \mathbf{B}_u, \quad \mathbf{T}_2 \triangleq \sum_{q=1}^Q \sum_{\substack{\tau=-P+1, \\ \tau \neq 0}}^{P-1} \mathbf{D}_{\tau,q,q}^H \mathbf{x} \mathbf{x}^H \mathbf{D}_{\tau,q,q}, \\ \mathbf{T}_3 & \triangleq \sum_{q=1}^{Q-1} \sum_{\substack{q'=1, \tau=-P+1 \\ q' \neq q}}^Q \sum_{\tau=-P+1}^{P-1} \mathbf{D}_{\tau,q,q'}^H \mathbf{x} \mathbf{x}^H \mathbf{D}_{\tau,q,q'}. \end{aligned}$$

Using these objective representations, the problem (11) can be rewritten as

$$\begin{aligned} \min_{\mathbf{x}, \mathbf{u}, \mathbf{v}, \{z_{\ell}\}_{\ell=1}^L} & g(\mathbf{x}) = \tilde{g}(\mathbf{v}) \\ \text{s.t.} & \Re\{z_{\ell,m}\} \geq \tilde{\Gamma}_m, \forall m, \ell \\ & |u_n| = 1, \forall n = 1, 2, \dots, LN_T \\ & \mathbf{x} = \mathbf{v}, \quad \mathbf{u} = \mathbf{v} \\ & z_{\ell,m} = \tilde{\mathbf{h}}_{\ell,m}^H \mathbf{x}, \forall m, \ell \end{aligned} \quad (15)$$

The scaled augmented Lagrangian function for (15) can be rewritten as

$$\begin{aligned} \mathcal{L}(\mathbf{x}, \mathbf{v}, \mathbf{u}, \mathbf{z}, \boldsymbol{\rho}, \boldsymbol{\eta}_1, \boldsymbol{\eta}_2) & = g(\mathbf{x}) \\ & + \frac{\mu_1}{2} (\|\mathbf{x} - \mathbf{v} + \boldsymbol{\eta}_1\|^2 - \|\boldsymbol{\eta}_1\|^2) \\ & + \frac{\mu_2}{2} (\|\mathbf{u} - \mathbf{v} + \boldsymbol{\eta}_2\|^2 - \|\boldsymbol{\eta}_2\|^2) \\ & + \frac{\mu_3}{2} \sum_{\ell=1}^L \sum_{m=1}^{2K} \left( \left| z_{\ell,m} - \tilde{\mathbf{h}}_{\ell,m}^H \mathbf{x} + \rho_{\ell,m} \right|^2 - |\rho_{\ell,m}|^2 \right), \end{aligned}$$

where  $\mu_1, \mu_2, \mu_3 \in \mathbb{R}^+$  are the scalar penalty parameters,  $\boldsymbol{\eta}_1, \boldsymbol{\eta}_2 \in \mathbb{C}^{LN_T \times 1}$  are the Lagrange multipliers for the equality constraints  $\mathbf{x} = \mathbf{v}$  and  $\mathbf{u} = \mathbf{v}$ , respectively,  $\mathbf{z} = [z_1^H, z_2^H, \dots, z_L^H]^H$ ,  $\rho_{\ell, m} \in \mathbb{C}$  is the Lagrange multiplier for the equality constraint  $z_{\ell, m} = \tilde{\mathbf{h}}_{\ell, m}^H \mathbf{x}$  for all  $\ell, m$ , and  $\boldsymbol{\rho} = [\boldsymbol{\rho}_1^H, \boldsymbol{\rho}_2^H, \dots, \boldsymbol{\rho}_L^H]^H$  is the Lagrange multiplier vector for the equality constraints with  $\boldsymbol{\rho}_\ell = [\rho_{\ell, 1}, \rho_{\ell, 2}, \dots, \rho_{\ell, 2K}]^H$ . Accordingly, the problem (15) can be decomposed into multiple subproblems and written in iterative form as

$$\mathbf{x}^{(i+1)} := \arg \min_{\mathbf{x}} \mathcal{L}(\mathbf{x}, [\mathbf{v}, \mathbf{u}, \mathbf{z}, \boldsymbol{\rho}, \boldsymbol{\eta}_1, \boldsymbol{\eta}_2]^{(i)}), \quad (16)$$

$$\mathbf{v}^{(i+1)} := \arg \min_{\mathbf{v}} \mathcal{L}(\mathbf{x}^{(i+1)}, \mathbf{v}, [\mathbf{u}, \mathbf{z}, \boldsymbol{\rho}, \boldsymbol{\eta}_1, \boldsymbol{\eta}_2]^{(i)}), \quad (17)$$

$$\mathbf{u}^{(i+1)} := \arg \min_{\mathbf{u} \in \mathcal{R}_u} \mathcal{L}([\mathbf{x}, \mathbf{v}]^{(i+1)}, \mathbf{u}, [\mathbf{z}, \boldsymbol{\rho}, \boldsymbol{\eta}_1, \boldsymbol{\eta}_2]^{(i)}), \quad (18)$$

$$z_{\ell, m}^{(i+1)} := \arg \min_{z_{\ell, m} \in \mathcal{R}_m} \mathcal{L}([\mathbf{x}, \mathbf{v}, \mathbf{u}]^{(i+1)}, \mathbf{z}, [\boldsymbol{\rho}, \boldsymbol{\eta}_1, \boldsymbol{\eta}_2]^{(i)}), \quad (19)$$

$$\boldsymbol{\eta}_1^{(i+1)} := \boldsymbol{\eta}_1^{(i)} + \mathbf{x}^{(i+1)} - \mathbf{v}^{(i+1)}, \quad (20)$$

$$\boldsymbol{\eta}_2^{(i+1)} := \boldsymbol{\eta}_2^{(i)} + \mathbf{u}^{(i+1)} - \mathbf{v}^{(i+1)}, \quad (21)$$

$$\rho_{\ell, m}^{(i+1)} := \rho_{\ell, m}^{(i)} + z_{\ell, m}^{(i+1)} - \tilde{\mathbf{h}}_{\ell, m}^H \mathbf{x}^{(i+1)}, \quad (22)$$

where  $i$  is the ADMM iteration index,  $\mathcal{R}_u = \{\mathbf{u} : |\mathbf{u}_n| = 1, \forall n = 1, 2, \dots, LN_T\}$ , and  $\mathcal{R}_m = \{z : \Re\{z\} \geq \tilde{\Gamma}_m\}$ .

#### B. Update of $\mathbf{x}^{(i+1)}$

The subproblem (16) is an unconstrained quadratic optimization.

**Lemma 1.** The closed-form solution to the subproblem (16) for  $\mathbf{x}$  can be obtained at the critical point, which is given by  $\mathbf{x}^* = \boldsymbol{\Omega}_1^{-1} \boldsymbol{\psi}_1$ , where

$$\boldsymbol{\Omega}_1 \triangleq \mathbf{G} + \frac{\mu_1}{2} \mathbf{I}_{LN_T} + \frac{\mu_3}{2} \sum_{\ell=1}^L \sum_{m=1}^{2K} \tilde{\mathbf{h}}_{\ell, m} \tilde{\mathbf{h}}_{\ell, m}^H,$$

$$\mathbf{G} \triangleq \omega_{bp} \mathbf{G}_1 + \omega_{ac} \mathbf{G}_2 + \omega_{cc} \mathbf{G}_3, \text{ and}$$

$$\boldsymbol{\psi}_1 \triangleq \frac{\mu_1}{2} (\mathbf{v}^{(i)} - \boldsymbol{\eta}_1^{(i)}) + \frac{\mu_3}{2} \sum_{\ell=1}^L \sum_{m=1}^{2K} \tilde{\mathbf{h}}_{\ell, m} (z_{\ell, m}^{(i)} + \rho_{\ell, m}^{(i)}).$$

See Appendix B for details of the proof.

#### C. Update of $\mathbf{v}^{(i+1)}$

Similar to the subproblem (16), the subproblem (17) for  $\mathbf{v}$  is an unconstrained quadratic problem, which is given by  $\min_{\mathbf{v}} \mathcal{L}(\mathbf{x}^{(i+1)}, \mathbf{v}, [\mathbf{u}, \mathbf{z}, \boldsymbol{\rho}, \boldsymbol{\eta}_1, \boldsymbol{\eta}_2]^{(i)})$ . The solution is given by the following lemma:

**Lemma 2.** The closed-form solution to the subproblem (17) for  $\mathbf{v}$  is given by  $\mathbf{v}^* = \boldsymbol{\Omega}_2^{-1} \boldsymbol{\psi}_2$ , where

$$\boldsymbol{\Omega}_2 \triangleq \mathbf{T} + \frac{\mu_1 + \mu_2}{2} \mathbf{I}_{LN_T}, \quad \mathbf{T} \triangleq \omega_{bp} \mathbf{T}_1 + \omega_{ac} \mathbf{T}_2 + \omega_{cc} \mathbf{T}_3,$$

$$\text{and, } \boldsymbol{\psi}_2 \triangleq \frac{\mu_1}{2} (\mathbf{x}^{(i+1)} + \boldsymbol{\eta}_1^{(i)}) + \frac{\mu_2}{2} (\mathbf{u}^{(i)} + \boldsymbol{\eta}_2^{(i)}).$$

See Appendix B for details of the proof.

#### D. Update of $z_{\ell, m}^{(i+1)}$

Next, ignoring the irrelevant variables, the subproblem (19) for the auxiliary variable  $z_{\ell, m}$  can be rewritten as

$$\min_{z_{\ell, m} \in \mathcal{R}_m} \left| z_{\ell, m} - \tilde{\mathbf{h}}_{\ell, m}^H \mathbf{x}^{(i+1)} + \rho_{\ell, m}^{(i)} \right|^2. \quad (23)$$

---

### Algorithm 1: Proposed ADMM-based Algorithm

---

- 1 **Input:** Initial point  $\mathbf{x}_0$ , stopping threshold  $\epsilon_1$
  - 2 **Initialize:**  $i \leftarrow 0$ ,  $g[i] = \infty$ ,  $\mathbf{x}^{(i)} = \mathbf{x}_0$ ,  
 $\boldsymbol{\eta}_1^{(i)} = \boldsymbol{\eta}_2^{(i)} = \mathbf{0}_{LN_T \times 1}$ ,  $\rho_{\ell, m}^{(i)} = 0$ ,  
 $z_{\ell, m}^{(i)} = \Re\{\tilde{\mathbf{h}}_{\ell, m}^H \mathbf{x}^{(i)}\}$ ,  $\mathbf{v}^{(i)} = \mathbf{x}^{(i)}$ ,  $\mathbf{u}^{(i)} = \mathbf{v}^{(i)}$
  - 3 **repeat**
  - 4     update  $\mathbf{x}^{(i+1)}$ ,  $\mathbf{v}^{(i+1)}$  and  $z_{\ell, m}^{(i+1)}$
  - 5     update  $\mathbf{u}^{(i+1)} \leftarrow e^{j\angle(\mathbf{v}^{(i+1)} - \boldsymbol{\eta}_2^{(i)})}$
  - 6     update  $\boldsymbol{\eta}_1^{(i+1)} \leftarrow \boldsymbol{\eta}_1^{(i)} + \mathbf{x}^{(i+1)} - \mathbf{v}^{(i+1)}$
  - 7     update  $\boldsymbol{\eta}_2^{(i+1)} \leftarrow \boldsymbol{\eta}_2^{(i)} + \mathbf{u}^{(i+1)} - \mathbf{v}^{(i+1)}$
  - 8     update  $\rho_{\ell, m}^{(i+1)} \leftarrow \rho_{\ell, m}^{(i)} + z_{\ell, m}^{(i+1)} - \tilde{\mathbf{h}}_{\ell, m}^H \mathbf{x}^{(i+1)}$
  - 9     set  $i \leftarrow i + 1$
  - 10     $g[i] \leftarrow \omega_{bp} \tilde{g}_{bp}(\mathbf{x}^{(i)}) + \omega_{ac} g_{ac}(\mathbf{x}^{(i)}) + \omega_{cc} g_{cc}(\mathbf{x}^{(i)})$
  - 11 **until**  $|g[i] - g[i-1]| / |g[i-1]| \leq \epsilon_1$ ;
  - 12 **Output:**  $\mathbf{X} = \text{mat}(\mathbf{x}^{(i)})$
- 

The above subproblem is convex due to the convex objective and constraint. Thus, the closed-form solution can be readily obtained from the Karush-Kuhn-Tucker (KKT) condition as

$$z_{\ell, m} = \begin{cases} \tilde{\mathbf{h}}_{\ell, m}^H \mathbf{x}^{(i+1)} - \rho_{\ell, m}^{(i)}, & \text{if } \Re\{\tilde{\mathbf{h}}_{\ell, m}^H \mathbf{x}^{(i+1)} - \rho_{\ell, m}^{(i)}\} \geq \tilde{\Gamma}_m \\ \tilde{\mathbf{h}}_{\ell, m}^H \mathbf{x}^{(i+1)} - \rho_{\ell, m}^{(i)} + \tilde{\Gamma}_m & \\ -\Re\{\tilde{\mathbf{h}}_{\ell, m}^H \mathbf{x}^{(i+1)} - \rho_{\ell, m}^{(i)}\} & \text{, otherwise.} \end{cases} \quad (24)$$

#### E. Update of $\mathbf{u}^{(i+1)}$

The subproblem (18) for the auxiliary variable  $\mathbf{u}$  can be simplified as

$$\min_{\mathbf{u}} \left\| \mathbf{u} - \mathbf{v}^{(i+1)} + \boldsymbol{\eta}_2^{(i)} \right\| \quad (25)$$

s.t.  $|u_n| = 1, \forall n = 1, 2, \dots, LN_T$ .

Next we state the following lemma, which was proven in [42].

**Lemma 3.** The solution to (25) is given by  $\mathbf{u}^{(i+1)} = e^{j\angle(\mathbf{v}^{(i+1)} - \boldsymbol{\eta}_2^{(i)})}$ .

The subproblems can be iteratively solved until the stopping criterion is satisfied. Then, we can recover the converged solution by reshaping the vector  $\mathbf{x}$  into the matrix  $\mathbf{X}$ , as described in Algorithm 1.

#### F. Complexity Analysis

We analyze the complexity of the proposed ADMM-based algorithm. The results are summarized in Table I. Each ADMM iteration requires updating variables  $\mathbf{x}, \mathbf{v}, \mathbf{u}, \mathbf{z}, \boldsymbol{\rho}, \boldsymbol{\eta}_1, \boldsymbol{\eta}_2$ . We assume  $Q \geq 2$  in our analysis. The solution  $\mathbf{x}^*$  to the first subproblem consists of the computation of  $\boldsymbol{\Omega}_1^{-1}$  and  $\boldsymbol{\psi}_1$ . The computation of  $\boldsymbol{\Omega}_1$  can be decomposed into the computations of  $\mathbf{G}_1, \mathbf{G}_2, \mathbf{G}_3$  and  $\sum_{m=1}^{2KL} \tilde{\mathbf{h}}_{\ell, m} \tilde{\mathbf{h}}_{\ell, m}^H$ . The computation of  $\mathbf{G}_1$  requires the evaluation of  $\mathbf{B}_u \mathbf{v} \mathbf{v}^H \mathbf{B}_u^H U$  times, which has complexity  $O(UL^2 N_T^2)$ . Matrices  $\mathbf{G}_2$  and  $\mathbf{G}_3$  can be computed similarly, with complexities  $O(Q(2P-1)L^2 N_T^2)$  and  $O(Q(Q-1)(2P-1)L^2 N_T^2/2)$ , respectively. The computation of  $\sum_{\ell=1}^L \sum_{m=1}^{2K} \tilde{\mathbf{h}}_{\ell, m} \tilde{\mathbf{h}}_{\ell, m}^H$  costs  $O(2KL^3 N_T^2)$ .

To sum up, the computation of  $\boldsymbol{\Omega}_1$  is  $O(UL^2 N_T^2 + Q^2 PL^2 N_T^2 + KL^3 N_T^2)$ . Also, since  $\boldsymbol{\Omega}_1$  is a  $LN_T \times LN_T$  matrix, its inversion costs  $O(L^3 N_T^3)$  assuming Gauss-Jordan

Table I: Complexity analysis of the ADMM-based Algorithm

Variable	Complexity
$\mathbf{x}^*$	$O(UL^2N_T^2 + Q^2PL^2N_T^2 + L^3N_T^3)$
$\mathbf{v}^*$	$O(UL^2N_T^2 + Q^2PL^2N_T^2 + L^3N_T^3)$
$\mathbf{z}^*, \boldsymbol{\rho}^*$	$O(L^2N_T^2)$
$\mathbf{u}^*, \boldsymbol{\eta}_1^*, \boldsymbol{\eta}_2^*$	$O(LN_T)$
Total	$O(UL^2N_T^2 + Q^2PL^2N_T^2 + L^3N_T^3)$

elimination methods. Calculating  $\boldsymbol{\psi}_1$  is dominated by the evaluation of  $\frac{\mu_3}{2} \sum_{\ell=1}^L \sum_{m=1}^{2K} \hat{\mathbf{h}}_{\ell,m}(z_{\ell,m} + \rho_{\ell,m})$ , which costs  $O(KL^2N_T)$ . Thus, we conclude that the computational cost of  $\mathbf{x}^*$  is given by  $O(UL^2N_T^2 + Q^2PL^2N_T^2 + L^3N_T^3)$ . Similar to  $\mathbf{x}^*$ , the solution  $\mathbf{v}^*$  to the second subproblem costs  $O(UL^2N_T^2 + Q(Q-1)(2P-1)L^2N_T^2 + L^3N_T^3)$ . Finally, the solution  $\mathbf{u}^*$  to the subproblem (25) requires a phase alignment operation, which costs  $O(LN_T)$ . Combining all the results, the computational complexity of each ADMM iteration is given by  $O(UL^2N_T^2 + Q^2PL^2N_T^2 + L^3N_T^3)$ .

#### IV. MM-BASED ALGORITHM

The ADMM-based solution discussed in Section III entails matrix inversion operations, which can be computationally inefficient for large block sizes. To overcome this, we develop an additional solution by leveraging the MM technique and the method of Lagrange multipliers. We first derive a linear majorizer of the fourth-order objective in (10) to handle its nonconvexity. The convergence speed of MM algorithms largely relies on the characteristic of the majorizing function [43]. With this in mind, we propose an improved majorizing function for quadratic functions that enhances convergence rates. With the proposed majorizer, the problem (10) can be approximated as a linear program with a constant modulus constraint. We decompose the approximated problem into multiple independent subproblems, which can be solved in parallel. In the following, we describe the majorization process of (10) and the solution based on dual problems.

##### A. Majorizing with an Improved Majorizer

To majorize the objective, we begin by rewriting the quadratic term in the beam pattern shaping cost as  $\mathbf{x}^H \mathbf{B}_u \mathbf{x} = \text{Tr}(\mathbf{x} \mathbf{x}^H \mathbf{B}_u) = \text{vec}^H(\mathbf{x} \mathbf{x}^H) \text{vec}(\mathbf{B}_u)$  [44]. Then, following the prevalent approach used in [14], [43]–[45], the fourth-order beam pattern shaping cost can be expressed as  $\sum_{u=1}^U |\mathbf{x}^H \mathbf{B}_u \mathbf{x}|^2 = \text{vec}^H(\mathbf{x} \mathbf{x}^H) \boldsymbol{\Psi}_1 \text{vec}(\mathbf{x} \mathbf{x}^H)$ , where

$$\boldsymbol{\Psi}_1 \triangleq \sum_{u=1}^U \text{vec}(\mathbf{B}_u) \text{vec}^H(\mathbf{B}_u).$$

It can be verified that  $\boldsymbol{\Psi}_1$  is an  $(L^2N_T^2 \times L^2N_T^2)$  Hermitian positive definite matrix. Following this approach, the objective can be expressed as

$$\begin{aligned} g(\mathbf{x}) &= \text{vec}^H(\mathbf{x} \mathbf{x}^H) \underbrace{(\omega_{bp} \boldsymbol{\Psi}_1 + \omega_{ac} \boldsymbol{\Psi}_2 + \omega_{cc} \boldsymbol{\Psi}_3)}_{\boldsymbol{\Psi}} \text{vec}(\mathbf{x} \mathbf{x}^H) \\ &= \text{vec}^H(\mathbf{x} \mathbf{x}^H) \boldsymbol{\Psi} \text{vec}(\mathbf{x} \mathbf{x}^H), \end{aligned} \quad (26)$$

where

$$\begin{aligned} \boldsymbol{\Psi}_2 &\triangleq \sum_{q=1}^Q \sum_{\substack{\tau=-P+1, \\ \tau \neq 0}}^{P-1} \text{vec}(\mathbf{D}_{\tau,q,q}) \text{vec}^H(\mathbf{D}_{\tau,q,q}); \\ \text{and } \boldsymbol{\Psi}_3 &\triangleq \sum_{q=1}^Q \sum_{\substack{q'=1, \\ q' \neq q}}^Q \sum_{\tau=-P+1}^{P-1} \text{vec}(\mathbf{D}_{\tau,q,q'}) \text{vec}^H(\mathbf{D}_{\tau,q,q'}). \end{aligned}$$

Then, we use the following lemma to construct a majorizer of the fourth-order objective function.

**Lemma 4.** [45, (13)] Let  $\mathbf{Q}, \mathbf{R}$  be Hermitian matrices with  $\mathbf{R} \succeq \mathbf{Q}$ . Then, a quadratic function  $\mathbf{u}^H \mathbf{Q} \mathbf{u}$  can be majorized at a point  $\mathbf{u}_t$  as

$$\mathbf{u}^H \mathbf{Q} \mathbf{u} \leq \mathbf{u}^H \mathbf{R} \mathbf{u} + 2\Re\{\mathbf{u}^H (\mathbf{Q} - \mathbf{R}) \mathbf{u}_t\} + \mathbf{u}_t^H (\mathbf{R} - \mathbf{Q}) \mathbf{u}_t.$$

According to the above lemma, we can majorize a quadratic function by choosing a matrix  $\mathbf{R}$  such that  $\mathbf{R} \succeq \mathbf{Q}$ . To simplify the right-hand side, matrix  $\mathbf{R}$  is required to be diagonal [46]. In the literature, the predominant choice for  $\mathbf{R}$  is  $\mathbf{R} = \lambda_Q \mathbf{I}$  where  $\lambda_Q$  is the largest eigenvalue of  $\mathbf{Q}$  [14], [43]–[45]. [46] proposed a novel diagonal matrix structure to enable tight majorization for the case where  $\mathbf{Q}$  is a non-negative symmetric matrix. This study demonstrated that a majorizer derived from their proposed diagonal matrix can accelerate the convergence speed significantly. Motivated by this, we propose a novel majorizer for quadratic functions with a complex Hermitian matrix based on the following lemma.

**Lemma 5.** Let  $\mathbf{Q}$  be a Hermitian matrix. Let  $\hat{\mathbf{Q}}$  be a matrix such that  $\hat{Q}_{i,j} = |Q_{i,j}|$ . Then,  $\text{diag}(\hat{\mathbf{Q}} \mathbf{1}) \succeq \mathbf{Q}$ .

*Proof.* For any  $\mathbf{u}$ , we have

$$\begin{aligned} \mathbf{u}^H (\text{diag}(\hat{\mathbf{Q}} \mathbf{1}) - \mathbf{Q}) \mathbf{u} &= \sum_{i,j} |Q_{i,j}| |u_i|^2 - \sum_{i,j} u_i^* Q_{i,j} u_j \\ &= \frac{1}{2} \sum_{i,j} (2|Q_{i,j}| |u_i|^2 - 2\Re\{Q_{i,j} u_i^* u_j\}) \\ &= \frac{1}{2} \sum_{i,j} (|Q_{i,j}| |u_i|^2 + |Q_{j,i}| |u_j|^2 - 2\Re\{Q_{i,j} u_i^* u_j\}) \\ &= \frac{1}{2} \sum_{i,j} (|Q_{i,j}| |u_i|^2 + |Q_{i,j}| |u_j|^2 - 2\Re\{Q_{i,j} u_i^* u_j\}), \end{aligned}$$

where the last equality follows from  $|Q_{i,j}| = |Q_{j,i}^*| = |Q_{j,i}|$ . Now, for any  $i, j$ , we have

$$\begin{aligned} &|Q_{i,j}| |u_i|^2 + |Q_{i,j}| |u_j|^2 - 2\Re\{Q_{i,j} u_i^* u_j\} \\ &\geq |Q_{i,j}| (|u_i| - |u_j|)^2 \geq 0, \end{aligned}$$

which follows from the fact that  $|Q_{i,j}| |u_i| |u_j| \geq \Re\{Q_{i,j} u_i^* u_j\}$ . It follows that  $\mathbf{u}^H (\text{diag}(\hat{\mathbf{Q}} \mathbf{1}) - \mathbf{Q}) \mathbf{u} \geq 0$ .  $\square$

Using Lemma 5, a tight majorizer for the beam shaping cost can be constructed as follows (with the proof in [34]).

**Lemma 6.** Let  $\hat{\boldsymbol{\Psi}}$  be a matrix such that  $\hat{\Psi}_{i,j} = |\Psi_{i,j}|$  for all  $i, j$ . The objective function (26) can be majorized as

$$g(\mathbf{x}) \leq \mathbf{x}^H \hat{\boldsymbol{\Psi}} \mathbf{x} + \text{const}, \quad (27)$$

where

$$\begin{aligned}\Phi &\triangleq 2(\omega_{bp}\Phi_1 + \omega_{ac}\Phi_2 + \omega_{cc}\Phi_3 - (\mathbf{E} \odot \mathbf{x}_t \mathbf{x}_t^H)), \\ \Phi_1 &\triangleq \sum_{u=1}^U \mathbf{x}_t^H \mathbf{B}_u^H \mathbf{x}_t \mathbf{B}_u, \Phi_2 \triangleq \sum_{q=1}^Q \sum_{\substack{\tau=-P+1 \\ \tau \neq 0}}^{P-1} \mathbf{x}_t^H \mathbf{D}_{\tau,q}^H \mathbf{x}_t \mathbf{D}_{\tau,q}, \\ \Phi_3 &\triangleq \sum_{q=1}^Q \sum_{\substack{q'=1 \\ q' \neq q}}^Q \sum_{\tau=-P+1}^{P-1} \mathbf{x}_t^H \mathbf{D}_{\tau,q}^H \mathbf{x}_t \mathbf{D}_{\tau,q'}, \mathbf{E} \triangleq \text{mat}(\hat{\Phi}\mathbf{1}).\end{aligned}$$

This majorizer is still quadratic, which is challenging to optimize under the constant modulus constraint. Thus, we further majorize the obtained quadratic function to lower its order as follows.

**Lemma 7.** Let  $\hat{\Phi}$  be a matrix such that  $\hat{\Phi}_{i,j} = |\Phi_{i,j}|$  for any  $i, j$ . The quadratic function on the right-hand side of (27) is majorized by

$$\mathbf{x}^H \Phi \mathbf{x} \leq \underbrace{\Re\{\mathbf{x}^H \mathbf{d}\}}_{\bar{g}(\mathbf{x})} + \text{const}, \quad (28)$$

where  $\mathbf{d} \triangleq 2(\Phi - \text{diag}(\hat{\Phi}\mathbf{1}))\mathbf{x}_t$ .

*Proof.* By applying Lemma 5 and Lemma 6, we have

$$\begin{aligned}\mathbf{x}^H \Phi \mathbf{x} &\leq \underbrace{\mathbf{x}^H \text{diag}(\hat{\Phi}\mathbf{1})\mathbf{x}}_{\mathbf{1}^T \hat{\Phi}\mathbf{1}} + \underbrace{\Re\{\mathbf{x}^H 2(\Phi - \text{diag}(\hat{\Phi}\mathbf{1}))\mathbf{x}_t\}}_{\mathbf{d}} \\ &+ \mathbf{x}_t^H (\text{diag}(\hat{\Phi}\mathbf{1}) - \Phi)\mathbf{x}_t = \Re\{\mathbf{x}^H \mathbf{d}\} + \text{const}.\end{aligned}$$

□

**Theorem 2.** Given the constant modulus constraint, the objective function can be majorized as

$$\omega_{bp}\tilde{g}_{bp}(\mathbf{x}) + \omega_{ac}g_{ac}(\mathbf{x}) + \omega_{cc}g_{cc}(\mathbf{x}) \leq \bar{g}(\mathbf{x}) + \text{const}, \quad (29)$$

where  $\bar{g}(\mathbf{x}) = \Re\{\mathbf{x}^H \mathbf{d}\} = \Re\{\mathbf{d}^H \mathbf{x}\}$ .

*Proof.* It follows from Lemmas 6 and 7. □

*B. Solution via the Method of Lagrange Multipliers*

Now, using (29), problem (10) can be reformulated as

$$\begin{aligned}\min_{\mathbf{x}} \quad & \Re\{\mathbf{d}^H \mathbf{x}\} \\ \text{s.t.} \quad & \Re\{\hat{\mathbf{h}}_{\ell,m}^H \mathbf{x}\} \geq \tilde{\Gamma}_m, \forall \ell, m \\ & |x_n| = 1, \forall n = 1, 2, \dots, LN_T\end{aligned} \quad (30)$$

The majorized objective can be rewritten as  $\Re\{\mathbf{d}^H \mathbf{x}\} = \sum_{\ell=1}^L \Re\{\mathbf{d}_\ell^H \mathbf{x}_\ell\}$ , where  $\mathbf{x}_\ell$  and  $\mathbf{d}_\ell$  are the  $\ell$ th subvectors of  $\mathbf{x} = [\mathbf{x}_1^H, \mathbf{x}_2^H, \dots, \mathbf{x}_L^H]^H$  and  $\mathbf{d} = [\mathbf{d}_1^H, \mathbf{d}_2^H, \dots, \mathbf{d}_L^H]^H$ , respectively. Also, from (8), we have  $\Re\{\hat{\mathbf{h}}_{\ell,m}^H \mathbf{x}\} = \Re\{\hat{\mathbf{h}}_{\ell,m}^H \mathbf{x}_\ell\}$ . Hence, the problem (30) can be rewritten as

$$\begin{aligned}\min_{\{\mathbf{x}_\ell\}_{\ell=1}^L} \quad & \sum_{\ell=1}^L \Re\{\mathbf{d}_\ell^H \mathbf{x}_\ell\} \\ \text{s.t.} \quad & \Re\{\hat{\mathbf{h}}_{\ell,m}^H \mathbf{x}_\ell\} \geq \tilde{\Gamma}_m, \forall \ell, m \\ & |x_{\ell,n}| = 1, \forall n = 1, 2, \dots, N_T\end{aligned} \quad (31)$$

where  $x_{\ell,n}$  is the  $n$ th entry of  $\mathbf{x}_\ell$ . Since  $\mathbf{x}_1, \mathbf{x}_2, \dots, \mathbf{x}_L$  are independent of each other in (31), the problem (31) can be split into  $L$  independent subproblems as

$$\begin{aligned}\min_{\mathbf{x}_\ell} \quad & \bar{g}_\ell(\mathbf{x}_\ell) \\ \text{s.t.} \quad & h_{\ell,m}(\mathbf{x}_\ell) \leq 0, \forall m = 1, 2, \dots, 2K \\ & |x_{\ell,n}| = 1, \forall n = 1, 2, \dots, N_T\end{aligned} \quad (32)$$

where  $\bar{g}_\ell(\mathbf{x}_\ell) = \Re\{\mathbf{d}_\ell^H \mathbf{x}_\ell\}$  and  $h_{\ell,m}(\mathbf{x}_\ell) = -\Re\{\hat{\mathbf{h}}_{\ell,m}^H \mathbf{x}_\ell\} + \tilde{\Gamma}_m$ . The Lagrange dual problem for (32) is given by

$$\begin{aligned}\sup_{\boldsymbol{\nu}_\ell} \min_{\mathbf{x}_\ell} \quad & \bar{g}_\ell(\mathbf{x}_\ell) + \sum_{m=1}^{2K} \nu_{\ell,m} h_{\ell,m}(\mathbf{x}_\ell) \\ \text{s.t.} \quad & |x_{\ell,n}| = 1, \forall n = 1, 2, \dots, N_T \\ & \nu_{\ell,m} \geq 0, \forall m, \ell\end{aligned} \quad (33)$$

where  $x_{\ell,n}$  is the  $n$ th entry of  $\mathbf{x}_\ell$  and  $\boldsymbol{\nu}_\ell = [\nu_{\ell,1}, \nu_{\ell,2}, \dots, \nu_{\ell,2K}]$  is the Lagrange multiplier vector with  $\nu_{\ell,m}$  being the Lagrange multiplier for the communication constraint  $h_{\ell,m}(\mathbf{x}_\ell) \leq 0$ . The inner problem of (33) has a linear objective with a constant modulus constraint. Thus, the optimal solution to the inner problem can be expressed as  $\mathbf{x}_\ell^*(\boldsymbol{\nu}_\ell) = \exp\left(j\angle\left(\sum_{m=1}^{2K} \nu_{\ell,m} \hat{\mathbf{h}}_{\ell,m} - \mathbf{d}_\ell\right)\right)$ .

Strong duality between the primal and dual problems holds [42] if there exists a solution  $\boldsymbol{\nu}_\ell$  that satisfies the following conditions:

$$\mathbf{x}_\ell(\boldsymbol{\nu}_\ell) = \exp\left(j\angle\left(\sum_{m=1}^{2K} \nu_{\ell,m} \hat{\mathbf{h}}_{\ell,m} - \mathbf{d}_\ell\right)\right), \quad (34)$$

$$0 \leq \nu_{\ell,m} \leq \infty, h_{\ell,m}(\mathbf{x}_\ell(\boldsymbol{\nu}_\ell)) \leq 0, \forall m = 1, 2, \dots, 2K \quad (35)$$

$$\nu_{\ell,m} h_{\ell,m}(\mathbf{x}_\ell(\boldsymbol{\nu}_\ell)) = 0, \forall m = 1, 2, \dots, 2K. \quad (36)$$

A solution satisfying (34) and (36) always exists, given  $\nu_{\ell,m} < \infty$  for all  $\ell, m$ . Assuming that the feasible set is strictly feasible, we have  $\lim_{\nu_{\ell,m} \rightarrow \infty} h_{\ell,m}(\mathbf{x}_\ell(\boldsymbol{\nu}_\ell)) = h_{\ell,m}\left(\exp\left(j\angle\hat{\mathbf{h}}_{\ell,m}\right)\right) < 0$  for any  $\ell, m$ . Hence, there exists finite  $\boldsymbol{\nu}_\ell$  that satisfies equation (36), leading to strong duality. Using this fact, we focus on solving the dual problem rather than directly solving the primal problem. Given the closed-form solution to the inner problem (34), the dual problem (33) can be reduced to finding optimal Lagrange multipliers  $\boldsymbol{\nu}_\ell$  that satisfy conditions (35) and (36). With this in mind, the dual problem can be reformulated as

$$\begin{aligned}\sup_{\boldsymbol{\nu}_\ell} \quad & \bar{g}_\ell(\boldsymbol{\nu}_\ell) + \sum_{m=1}^{2K} \nu_{\ell,m} h_{\ell,m}(\boldsymbol{\nu}_\ell) \\ \text{s.t.} \quad & \nu_{\ell,m} \geq 0, h_{\ell,m}(\boldsymbol{\nu}_\ell) \leq 0, \forall m = 1, 2, \dots, 2K \\ & \nu_{\ell,m} h_{\ell,m}(\boldsymbol{\nu}_\ell) = 0, \forall m = 1, 2, \dots, 2K\end{aligned} \quad (37)$$

For ease of notation,  $\bar{g}_\ell(\mathbf{x}_\ell(\boldsymbol{\nu}_\ell))$  and  $h_{\ell,m}(\mathbf{x}_\ell(\boldsymbol{\nu}_\ell))$  are denoted by  $\bar{g}_\ell(\boldsymbol{\nu}_\ell)$  and  $h_{\ell,m}(\boldsymbol{\nu}_\ell)$ , respectively.

The problem (37) can be solved via a coordinate ascent method where one Lagrange multiplier is optimized at a time with the other Lagrange multipliers fixed. For updating each coordinate, we use a modified version of the bisection algorithm in [42], as described in Algorithm 2. Once the Lagrange multiplier  $\nu_\ell$  is obtained,  $\mathbf{x}_\ell$  can be recovered using (34). Note that  $\mathbf{x}_1, \mathbf{x}_2, \dots, \mathbf{x}_L$  can be updated in parallel to accelerate the algorithm. The solution  $\mathbf{x}_t$  for the  $t$ -th MM iteration can be obtained by concatenating the subvectors as  $\mathbf{x}_t = [\mathbf{x}_1^H, \mathbf{x}_2^H, \dots, \mathbf{x}_L^H]^H$ . This iterative process continues until the objective value converges. The final converged solution can be reshaped into a matrix as  $\mathbf{X} = \text{mat}(\mathbf{x}_t)$ . The overall iterative solution is described in Algorithm 3.



---

**Algorithm 2:**  $2K$ -Dimension Bisection Method for Finding Dual Variables

---

```

1 Input: Lagrange multiplier vector  $\boldsymbol{\nu}_\ell$ , stopping
  thresholds  $\epsilon_2, \epsilon_3$ 
2 Initialization:  $i = 0; \boldsymbol{\nu}_\ell[0] = \boldsymbol{\nu}_\ell, \hat{g}_\ell[0] = \infty$ ; With
  slight abuse of notation,  $h_{\ell,m}(\boldsymbol{\nu}')$  denotes
   $h_{\ell,m}(\boldsymbol{\nu}_\ell)|_{\boldsymbol{\nu}_{\ell,m}=\boldsymbol{\nu}'}$ 
3 repeat
4   for  $m = 1 : 2K$  do
5     if  $h_{\ell,m}(0) \leq 0$  then  $\boldsymbol{\nu}^u = 0$ 
6     else
7        $\boldsymbol{\nu}^l = 0, \boldsymbol{\nu}^u = 1$ ;
8       if  $h_{\ell,m}(\boldsymbol{\nu}^u) \leq 0$  then  $\boldsymbol{\nu}^u = 1$ 
9       else
10        repeat  $\boldsymbol{\nu}^u = 2\boldsymbol{\nu}^u$  until  $h_{\ell,m}(\boldsymbol{\nu}^u) \leq 0$ 
11         $\boldsymbol{\nu}^l = \boldsymbol{\nu}^u/2$ 
12        repeat
13           $\boldsymbol{\nu}_{\ell,m} = (\boldsymbol{\nu}^l + \boldsymbol{\nu}^u)/2$ ;
14          if  $h_{\ell,m}(\boldsymbol{\nu}_{\ell,m}) > 0$  then  $\boldsymbol{\nu}^l = \boldsymbol{\nu}_{\ell,m}$ 
15          else  $\boldsymbol{\nu}^u = \boldsymbol{\nu}_{\ell,m}$ 
16        until  $|h_{\ell,m}(\boldsymbol{\nu}_{\ell,m}) + \epsilon_3/2| < \epsilon_3/2$ 
17      Update  $i \leftarrow i + 1$ , set  $\boldsymbol{\nu}_\ell[i] = [\nu_1, \dots, \nu_{2K}]$ 
18      Update  $\hat{g}_\ell[i] = \bar{g}_\ell(\boldsymbol{\nu}_\ell[i]) + \sum_{m=1}^{2K} \nu_{\ell,m} h_{\ell,m}(\boldsymbol{\nu}_\ell[i])$ 
19 until  $|\hat{g}_\ell[i] - \hat{g}_\ell[i-1]|/|\hat{g}_\ell[i-1]| < \epsilon_2$ 
20 Output: Recover a solution  $\boldsymbol{x}$  from  $\boldsymbol{\nu}[i]$  and (34)

```

---



---

**Algorithm 3:** Proposed MM-based Algorithm

---

```

1 Input: Initial point  $\boldsymbol{x}_0$ , stopping threshold  $\epsilon_4$ 
2 Initialize: Set  $t = 0, \boldsymbol{x}^{(t)} = \boldsymbol{x}_0, g[t] = \infty$ 
3 repeat
4    $t \leftarrow t + 1$ 
5   Update  $\boldsymbol{x}_1, \dots, \boldsymbol{x}_L$  using (29) and Algorithm 2
6    $\boldsymbol{x}^{(t)} \leftarrow [\boldsymbol{x}_1^H, \boldsymbol{x}_2^H, \dots, \boldsymbol{x}_L^H]^H$ 
7    $g[t] \leftarrow \omega_{bp} \hat{g}_{bp}(\boldsymbol{x}^{(t)}) + \omega_{ac} g_{ac}(\boldsymbol{x}^{(t)}) + \omega_{cc} g_{cc}(\boldsymbol{x}^{(t)})$ 
8 until  $|g[t] - g[t-1]|/|g[t-1]| \leq \epsilon_4$ 
9 Output:  $\mathbf{X} = \text{mat}(\boldsymbol{x}^{(t)})$ 

```

---

**C. Complexity Analysis**

Now we analyze the complexity of our proposed MM-based algorithm. The proposed MM-based algorithm comprises the majorization process and the bisection algorithm for solving the dual problem. The majorization process involves computation of the matrices  $\boldsymbol{\Psi}$ ,  $\boldsymbol{\Phi}$ , and the vector  $\mathbf{d}$ . The matrix  $\boldsymbol{\Psi}$  can be precomputed since it is independent of variable  $\boldsymbol{x}_t$ . Thus, we focus on analyzing the complexity of computing  $\boldsymbol{\Phi}$  and  $\mathbf{d}$ . The computation of  $\boldsymbol{\Phi}$  requires the computations of  $\boldsymbol{\Phi}_1, \boldsymbol{\Phi}_2, \boldsymbol{\Phi}_3$ . The matrix  $\boldsymbol{\Phi}_1$  is the sum of  $\boldsymbol{x}_t^H \mathbf{B}_u^H \boldsymbol{x}_t \mathbf{B}_u$  for  $u = 1, \dots, U$ . The evaluation of  $\boldsymbol{x}_t^H \mathbf{B}_u^H \boldsymbol{x}_t \mathbf{B}_u$  involves matrix multiplications, which takes the computational cost  $O(L^2 N_T^2)$ . Thus, the complexity of  $\boldsymbol{\Phi}_1$  is  $O(UL^2 N_T^2)$ . Following the same approach, the computational complexities of  $\boldsymbol{\Phi}_2$  and  $\boldsymbol{\Phi}_3$  can be obtained as  $O(Q(2P-1)L^2 N_T^2)$  and  $O(Q(Q-1)(2P-1)L^2 N_T^2/2)$ , respectively. The computation of  $\mathbf{d}$  involves evaluating  $2(\boldsymbol{\Phi} - \text{diag}(\hat{\boldsymbol{\Phi}}))\boldsymbol{x}_t$ , which costs  $O(L^2 N_T^2)$ . Thus, the overall computational complexity of the majorization

Table II: Complexity analysis of the MM-based algorithm

Variable	Complexity
$\boldsymbol{\Phi}_1$	$O(UL^2 N_T^2)$
$\boldsymbol{\Phi}_2$	$O(QPL^2 N_T^2)$
$\boldsymbol{\Phi}_3$	$O(Q^2 PL^2 N_T^2)$
$\mathbf{d}$	$O(L^2 N_T^2)$
Total	$O(UL^2 N_T^2 + Q^2 PL^2 N_T^2)$

process cost can be expressed as  $O(UL^2 N_T^2 + Q^2 PL^2 N_T^2)$ . We summarize the computational complexity of the above variables in Table II.

Next, we analyze the complexity of the bisection algorithm. The bisection algorithm requires the evaluation of  $h_{\ell,m}(\boldsymbol{\nu}_\ell)$ , which costs  $O(N^2)$ . The considered bisection method terminates when the constraint  $h_{\ell,m}(\boldsymbol{\nu}_\ell)$  sufficiently approaches zero. This differs from the traditional bisection method that terminates when the length of the search interval falls below a threshold. Thus, it is difficult to acquire an analytical bound of the worst-case iteration number due to the nonlinear relationship between  $h_{\ell,m}(\boldsymbol{\nu}_\ell)$  and the Lagrange multiplier. However, the combination of MM and the considered bisection methods have empirically shown superior convergence rates to the penalty convex-concave procedure (CCP) method and semi-definite relaxation (SDR) [42].

Assuming full parallelization, the complexity of the bisection method will not increase with the block size  $L$ . Moreover, the MM-based solution avoids matrix inversion operations, whose complexity increases cubically with  $L$ . This allows the MM-based solution to converge faster than the ADMM-based solution developed in Section III when the block size is large, as we will see in Section V.

## V. SIMULATION RESULTS

### A. Simulation Setup

In this section, we evaluate the proposed algorithms through simulations. We use the following setting unless otherwise specified. The waveform contains 32 subpulses, i.e.,  $L = 32$ , and the largest range bin of interest is  $P = 8$  [35]. Also, the transmit power is  $P_T = 1$  and the noise variance for the communication users  $\sigma^2 = 0.01$  [22]. The transmit array is equipped with  $N_T = 10$  antennas with half-wavelength spacing [22]. We consider the uncorrelated Rayleigh channel for the communication channel of each user. We use 40 channel realizations to evaluate the average performance of the proposed algorithms unless otherwise specified. We set the discretized angle range to be  $[0^\circ, 180^\circ]$  with the angle resolution of  $0.5^\circ$ , i.e.,  $\theta_u = (u/2)^\circ$  for  $u = 1, 2, \dots, 360$ . For the reference beam pattern, we consider a rectangular beam pattern, which is given by

$$G_d(\theta) = \begin{cases} 1, & \text{if } \theta_q - \Delta_\theta/2 \leq \theta \leq \theta_q + \Delta_\theta/2 \forall q, \\ 0, & \text{otherwise,} \end{cases} \quad (38)$$

where  $\Delta_\theta$  is the beam width. We consider two target directions, i.e.,  $Q = 2$  each at angles  $\theta_1 = -30^\circ$  and  $\theta_3 = 40^\circ$ . The beam width  $\Delta_\theta$  is set to  $20^\circ$ . The weights for the cost functions are  $(\omega_{bp}, \omega_{ac}, \omega_{cc}) = (1, 4, 4)$ . The termination thresholds are set to  $\epsilon_1 = 10^{-4}$ ,  $\epsilon_2 = \epsilon_3 = 10^{-4}$ , and  $\epsilon_4 = 3 \times 10^{-6}$ . We configure the penalty parameters for the ADMM algorithm as  $\mu_1 = \mu_2 = 5 \times 10^3$  and  $\mu_3 = 1.5 \times 10^4$ .

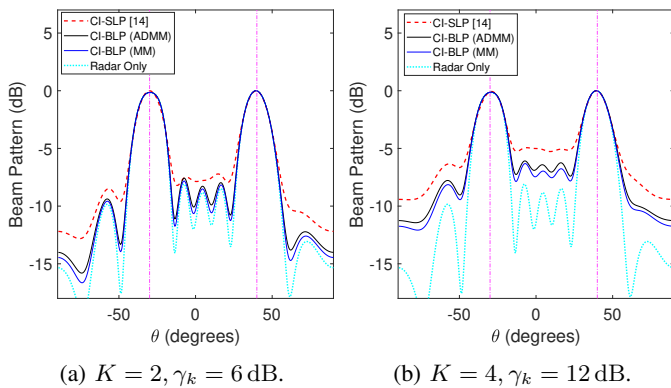


Figure 3: Synthesized beam patterns for two communication parameter sets. The vertical lines indicate the target angles. The proposed algorithms show beam patterns that are closer to those of the radar-only scheme than CI-SLP in the sidelobes.

For baselines, we use a radar-only scheme that solves (10) without the communication constraints, to verify the radar-communication trade-off. Also, we compare the proposed algorithm to the algorithm in [14], which optimizes the beam pattern shaping cost on a symbol-by-symbol basis, as opposed to our block-by-block strategy, under a per-user CI constraint. For clarity, we refer to our proposed scheme and the CI-SLP approach in [14] as CI-BLP and CI-SLP, respectively.

### B. Comparison of Beam Patterns

Figs. 3a and 3b compare the beam patterns designed by the proposed algorithms, the CI-SLP approach [14], and the radar-only scheme, for  $K = 2, \gamma_k = 6$  dB and  $K = 4, \gamma_k = 12$  dB. For both communication configurations, the radar-only scheme outperforms DFRC schemes in beam pattern approximation because it has no communication constraints. When  $K = 2, \gamma_k = 6$  dB, the beam patterns of the CI-BLP methods approach that of the radar-only scheme, while the CI-SLP method suffers from relatively higher sidelobe levels. The CI-SLP approach focuses on the symbol-by-symbol beam pattern shaping, which can be seen as a myopic approach. In contrast, the CI-BLP approach optimizes the beam pattern on a block level, resulting in lower spatial sidelobes. When  $K = 4, \gamma_k = 12$  dB, we observe a similar trend where the proposed approach maintains lower sidelobes than the CI-SLP approach. The overall sidelobes levels increased compared to the previous figure, except for the radar-only scheme. This suggests that the difficulty of beam pattern shaping increases as communication requirements become more demanding. Additionally, our improvement over CI-SLP is more pronounced in this case. For both cases, the MM-based solution slightly outperforms the ADMM-based solution in terms of beam pattern approximation, leading to higher spatial resolution.

### C. Autocorrelation and Cross-Correlation Properties

Next, we evaluate the waveform correlation properties using the same setup described in Section V-B. Figs. 4 and 5 plot the autocorrelation and cross-correlation performance of the proposed method and baselines. In all cases, the radar-only scheme outperforms the DFRC schemes in autocorrelation and cross-correlation, for the same reason as Fig. 3. The CI-SLP approach demonstrates the highest autocorrelation/cross-correlation sidelobe levels since it does not address waveform

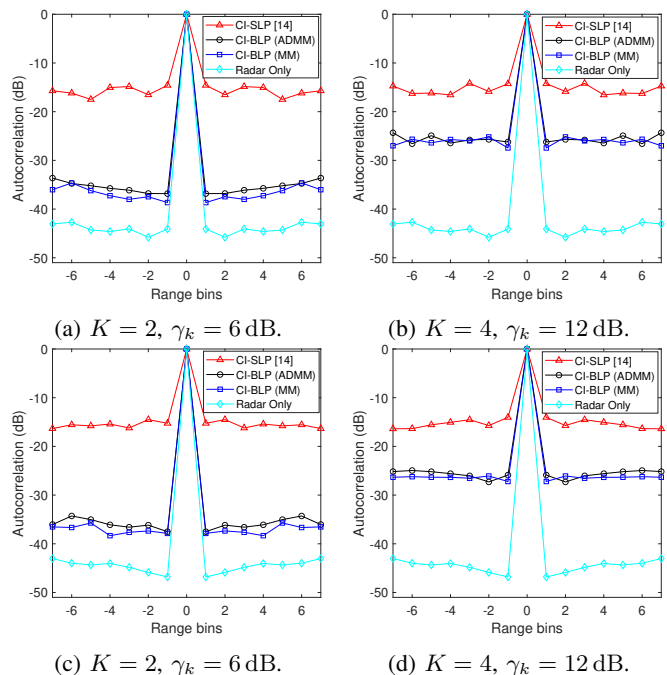


Figure 4: Autocorrelation at target angles (4a)(4b)  $\theta_1 = -30^\circ$  and (4c)(4d)  $\theta_2 = 40^\circ$  for two communication parameter sets. The CI-BLP approach reduces autocorrelations by approximately 20dB when  $K = 2, \gamma_k = 6$  dB and 10dB when  $K = 4, \gamma_k = 12$  dB, compared to the CI-SLP baseline.

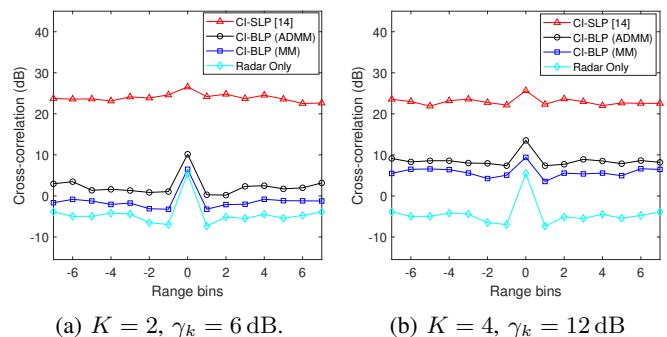


Figure 5: Cross-correlation between  $\theta_1 = -30^\circ$  and  $\theta_2 = 40^\circ$  for two communication parameter sets. The CI-BLP approach reduces cross-correlations by approximately 30dB when  $K = 2, \gamma_k = 6$  dB and 15dB when  $K = 4, \gamma_k = 12$  dB, compared to the CI-SLP approach.

correlations. In contrast, the proposed CI-BLP approach effectively reduces sidelobes owing to block-level ISL minimization. It is important to note that the CI-BLP approach nearly matches the sidelobe suppression performance of the radar-only scheme when  $K = 2, \gamma_k = 6$  dB, yielding a roughly 25 dB sidelobe reduction compared to the CI-SLP scheme. When  $K = 4, \gamma_k = 12$  dB, the overall sidelobe levels of the CI-BLP approach increase by 5 dB to 10 dB. This implies suppressing sidelobes becomes harder as the communication requirements become tighter, accounting for the radar-communication trade-off. Despite this, the CI-BLP approach outperforms the CI-SLP approach in terms of correlation for any configuration. Additionally, the MM-based solution achieves slightly lower sidelobe levels than the ADMM-based solution, consistent with the beam pattern results.

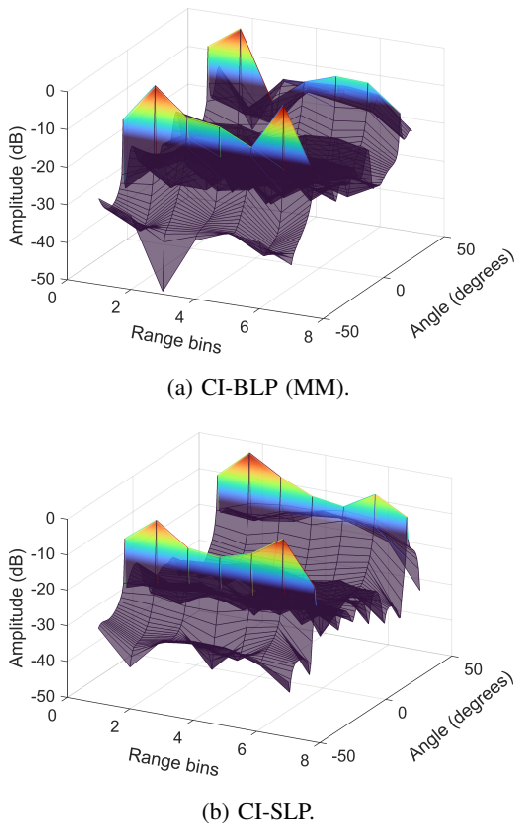


Figure 6: Capon spectral estimates of the CI-BLP and CI-SLP waveforms in the angle and range domain for  $K = 2$  and  $\Gamma = 6$  dB. The CI-BLP method obtains lower false alarms than the CI-SLP method due to the joint beam pattern and correlation optimization.

#### D. Capon Spectrum

We use the Capon method [47] to assess the positioning performance of the CI-BLP waveform. For the CI-BLP method, we use the waveform obtained through the MM-based algorithm. For each angle-range pair, we averaged the Capon estimates over 1000 noise realizations per channel realization. We configured three targets at  $(\theta_1, \tau_1) = (-30, 2)$ ,  $(\theta_2, \tau_2) = (-30, 6)$ , and  $(\theta_3, \tau_3) = (40, 2)$ . Also, the complex amplitude  $\kappa_q$  of the echo signal of target  $q$  is set to one, i.e.,  $\kappa_q = 1$ . The array signal-to-noise ratio (ASNR) [48] is set to 40 dB. Figs. 6a and 6b illustrate the Capon estimates at different angle and range bins, generated by the CI-BLP and CI-SLP waveforms, respectively, for  $K = 2$  and  $\Gamma = 6$  dB. All values are normalized to the maximum Capon amplitude and then converted to the dB scale. It can be observed that strong peaks form at the target locations in both cases due to the echoes reflected by the targets. The distinction between the two schemes is prominent at the range bins with no targets. The CI-SLP approach yields higher strengths at those range bins than the CI-BLP approach, which translates into higher false alarm rates. Conversely, the proposed CI-BLP approach attains lower intensity owing to the autocorrelation and cross-correlation sidelobe suppression. Overall, this suggests that our joint beam pattern and correlation optimization results in higher imaging resolutions and lower false alarms, especially in the multi-target scenario.

#### E. Cost Functions for Different QoS Parameters

To gain a better understanding of the radar-communication trade-off, we compared the beam pattern shaping cost  $g_{bp}(\mathbf{x})$ , autocorrelation ISL cost  $g_{ac}(\mathbf{x})$ , and cross-correlation ISL cost  $g_{cc}(\mathbf{x})$  for different QoS thresholds between 2 dB and 12 dB, and two different numbers of users  $K = 2$  and  $K = 4$ .

Fig. 7a demonstrates the beam shaping cost for different SINR thresholds. For all cases, the beam pattern shaping cost tends to increase as the QoS threshold increases due to the radar-communication trade-off. Likewise, the beam pattern costs appear higher when  $K = 4$  than  $K = 2$ , which confirms the previous discussions on the radar-communication trade-off. The proposed algorithms achieve lower beam pattern MSEs than the CI-SLP approach owing to block-level optimization. Moreover, we see the MM-based solution once again outperforms the ADMM-based solution for both  $K = 2$  and  $K = 4$ .

Figs. 7b and 7c demonstrate the autocorrelation and cross-correlation ISLs with increasing QoS thresholds, respectively. It can be verified that the proposed algorithms outperform the CI-SLP approach in correlation sidelobe levels for all cases. The autocorrelation and cross-correlation ISLs of the CI-SLP approach do not vary notably over different QoS thresholds because it does not address ISL minimization. Interestingly, the CI-SLP approach consistently shows lower autocorrelation and cross-correlation ISLs when  $K = 4$  than  $K = 2$ . This is an outcome of the reduction of the mainlobe power, not of the correlation minimization. For the CI-BLP scheme, we see increasing trends in autocorrelation and cross-correlation ISL. Moreover, the CI-BLP approach is about 7 dB higher in autocorrelation and cross-correlation ISL when  $K = 4$  than  $K = 2$ . This implies a potential degradation in target separation and positioning, particularly when the number of users is larger or the QoS threshold is high. Similar to the beam pattern results, the MM-based solution consistently outperforms the ADMM-based solution in autocorrelation and cross-correlation ISLs.

#### F. Convergence of the Proposed Algorithms

Fig. 8 compares the convergence properties of (1) the MM-based algorithm with the proposed majorizer, (2) the MM-based algorithm with a largest eigenvalue-based majorizer, and (3) the proposed ADMM algorithm, for  $K = 2$  and  $\gamma_k = 6$  dB, with two block sizes  $L = 8$  and  $L = 32$ . The proposed majorizer significantly increases the speed of convergence when compared to the largest eigenvalue majorizer. Moreover, consistent with the theory in [42], the MM-based algorithm shows a monotonic decrease in the objective value. Conversely, the ADMM algorithm shows spikes in the first few iterations before converging. This is caused by the alternating updates of the auxiliary variables, including dual ascents. The ADMM-based algorithm outperforms the MM-based algorithm in convergence speed for  $L = 8$ , while for  $L = 32$  the converse is true. The ADMM-based algorithm involves matrix inversions to solve quadratic subproblems, which costs  $O(L^3 N_T^3)$  as discussed in Section III-F, dominating convergence speed as the block size grows. In contrast, the per-iteration complexity of the MM-based algorithm is  $O((U + Q^2 P)L^2 N_T^2)$  as discussed in Section IV-C, which

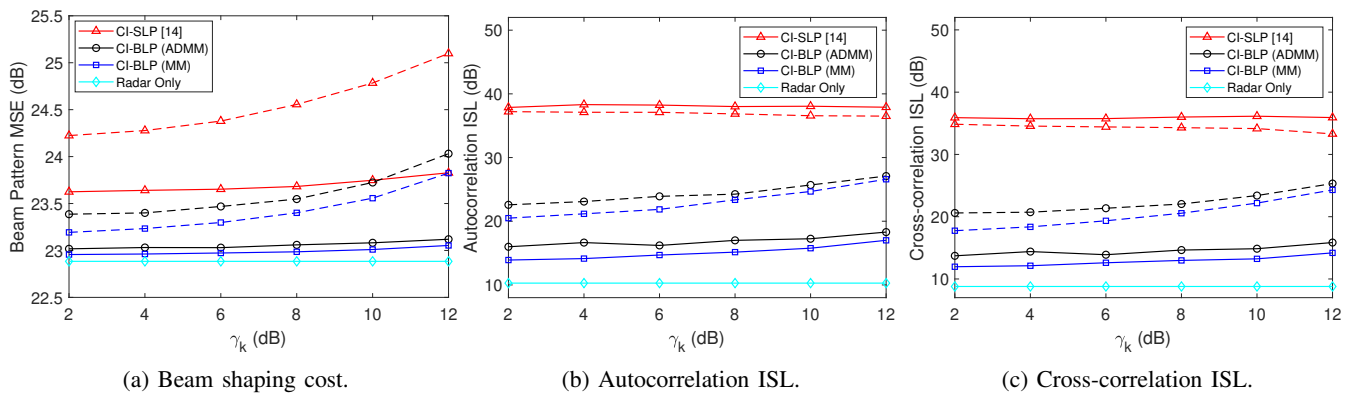


Figure 7: (7a) Beam pattern shaping, (7b) autocorrelation ISL, and (7c) cross-correlation ISL costs vs QoS threshold. The solid and dashed lines indicate the cases when  $K = 2$  and  $K = 4$  respectively.

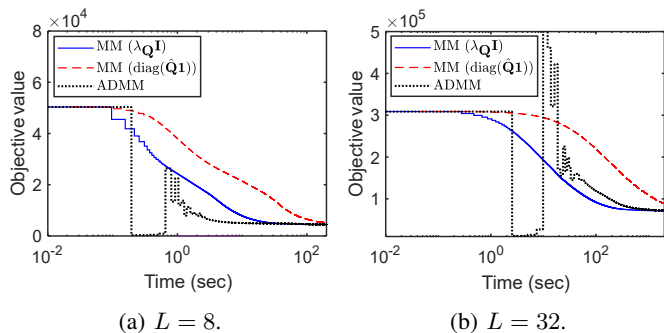


Figure 8: Convergence of the proposed algorithms for  $K = 2$  and  $\gamma_k = 6$  dB with two codeword lengths  $L = 8$  and  $L = 32$ .  $\lambda_Q \mathbf{I}$  and  $\text{diag}(\hat{\mathbf{Q}}\mathbf{1})$  denote the results of the largest eigenvalue and proposed majorizers, respectively. The ADMM-based algorithm outperforms the MM-based one for  $L = 8$ , while the converse is true for  $L = 32$ .

increases quadratically in  $L$ . Moreover, the complexity of the bisection search remains the same as the block size  $L$  grows large when fully parallelized. Consequently, the convergence speed of the ADMM-based algorithm decays faster than that of the MM-based algorithm as the block size increases.

## VI. CONCLUSION

This paper investigated the design of DFRC waveforms based on block-level optimization. We jointly optimized the spatial beam pattern and space-time correlations of the waveform for high-precision positioning. For communication, we employed a CI-BLP approach for block-level interference exploitation. To solve the formulated problem, we developed two algorithms, based on ADMM and MM techniques, which are suitable for small and large block sizes, respectively. Moreover, we proposed an improved majorizer for quadratic functions with a complex Hermitian matrix for faster convergence. Simulation results showed that block-level optimized waveforms outperform symbol-level optimized waveforms in terms of spatial and temporal sidelobe levels, significantly enhancing radar resolution. A possible future work could explore the design of low-complexity precoding schemes for DFRC systems, which can be crucial for practical implementations.

## APPENDIX A PROOF OF THEOREM 1

To show the nonconvexity of the feasible set, we transform the constraints in (10) into a real-valued constraint as

$$\bar{\mathbf{h}}_m^T \bar{\mathbf{x}} \geq \tilde{\Gamma}_m \quad \forall m, \quad \bar{x}_n^2 + \bar{x}_{n+LN_T}^2 = 1 \quad \forall n, \quad (39)$$

where  $\bar{\mathbf{x}} = [\Re\{\mathbf{x}^T\}, \Im\{\mathbf{x}^T\}]^T$  and  $\bar{\mathbf{h}}_m = [\Re\{\tilde{\mathbf{h}}_m^T\}, \Im\{\tilde{\mathbf{h}}_m^T\}]^T$ . The feasible region of the constant modulus constraint takes the shape of a unit circle in the  $n$ th and  $(n + LN_T)$ th coordinates. Moreover, the intersection of the linear communication constraints forms a polygon in the same coordinates. Consequently, the intersection of the feasible sets turns out to be an arc of each circle. Thus, the feasible set is nonconvex, which proves the problem (10) is nonconvex and NP-hard.

## APPENDIX B PROOF OF LEMMAS 1 AND 2

Since the first subproblem is an unconstrained quadratic problem, the solution can be found at the critical point. To find the critical point, we first compute the gradient of the objective as

$$\begin{aligned} & \nabla_{\mathbf{x}} \mathcal{L}(\mathbf{x}, \mathbf{u}, \mathbf{v}, \mathbf{z}, \boldsymbol{\rho}, \boldsymbol{\eta}_1, \boldsymbol{\eta}_2) \\ &= 2 \left( \mathbf{G} + \frac{\mu_1}{2} \mathbf{I}_{LN_T} + \frac{\mu_3}{2} \sum_{\ell=1}^L \sum_{m=1}^{2K} \tilde{\mathbf{h}}_{\ell,m} \tilde{\mathbf{h}}_{\ell,m}^H \right) \mathbf{x} \\ & - 2 \left( \frac{\mu_1}{2} (\mathbf{v} - \boldsymbol{\eta}_1) + \frac{\mu_3}{2} \sum_{\ell=1}^L \sum_{m=1}^{2K} \tilde{\mathbf{h}}_{\ell,m} (z_{\ell,m} + \rho_{\ell,m}) \right) \\ &= 2\boldsymbol{\Omega}_1 \mathbf{x} - 2\boldsymbol{\psi}_1. \end{aligned}$$

Here,  $\boldsymbol{\Omega}_1$  is a  $LN_T \times LN_T$  positive definite matrix since  $\omega_{bp} \mathbf{T}_1$ ,  $\omega_{ac} \mathbf{G}_1$ ,  $\omega_{cc} \mathbf{R}_1$ , and  $\frac{\mu_3}{2} \sum_{\ell=1}^L \sum_{m=1}^{2K} \tilde{\mathbf{h}}_{\ell,m} \tilde{\mathbf{h}}_{\ell,m}^H$  are positive definite. Hence, the optimal  $\mathbf{x}^*$  is obtained when the gradient is zero, i.e.,  $\boldsymbol{\Omega}_1 \mathbf{x} - \boldsymbol{\psi}_1 = 0$ . It follows that  $\mathbf{x}^* = \boldsymbol{\Omega}_1^{-1} \boldsymbol{\psi}_1$ . Similarly, to compute  $\mathbf{y}^*$ , we compute the gradient of the augmented Lagrangian with respect to  $\mathbf{y}$  as

$$\begin{aligned} & \nabla_{\mathbf{y}} \mathcal{L}(\mathbf{x}, \mathbf{u}, \mathbf{v}, \mathbf{z}, \boldsymbol{\rho}, \boldsymbol{\eta}_1, \boldsymbol{\eta}_2) = 2 \left( \mathbf{T} + \frac{\mu_1 + \mu_2}{2} \mathbf{I}_{LN_T} \right) \mathbf{y} \\ & - 2 \left( \frac{\mu_1}{2} (\mathbf{x} + \boldsymbol{\eta}_1) + \frac{\mu_2}{2} (\mathbf{u} + \boldsymbol{\eta}_2) \right) = 2\boldsymbol{\Omega}_2 \mathbf{y} - 2\boldsymbol{\psi}_2, \end{aligned}$$

where  $\boldsymbol{\Omega}_2$  is a  $LN_T \times LN_T$  positive definite matrix. Thus, the solution  $\mathbf{y}^*$  is obtained as  $\mathbf{y}^* = \boldsymbol{\Omega}_2^{-1} \boldsymbol{\psi}_2$ .

## REFERENCES

- [1] F. Liu, C. Masouros, A. P. Petropulu, H. Griffiths, and L. Hanzo, "Joint radar and communication design: Applications, state-of-the-art, and the road ahead," *IEEE Trans. Commun.*, vol. 68, no. 6, pp. 3834–3862, 2020.
- [2] A. Kaushik, R. Singh, S. Dayarathna, R. Senanayake, M. Di Renzo, M. Dajer, H. Ji, Y. Kim, V. Sciancalepore, A. Zappone *et al.*, "Towards integrated sensing and communications for 6g: A standardization perspective," *arXiv preprint arXiv:2308.01227*, 2023.
- [3] F. Liu, Y. Cui, C. Masouros, J. Xu, T. X. Han, Y. C. Eldar, and S. Buzzi, "Integrated sensing and communications: Towards dual-functional wireless networks for 6G and beyond," *IEEE J. Sel. Areas Commun.*, 2022.
- [4] D. Ying, D. J. Love, and B. M. Hochwald, "Transmit covariance optimization with a constraint on user electromagnetic radiation exposure," in *IEEE Global Communications Conference (GLOBECOM)*, 2013, pp. 4104–4109.
- [5] F. Liu, C. Masouros, A. Li, H. Sun, and L. Hanzo, "MU-MIMO communications with MIMO radar: From co-existence to joint transmission," *IEEE Trans. Wireless Commun.*, vol. 17, no. 4, pp. 2755–2770, 2018.
- [6] F. Liu, L. Zhou, C. Masouros, A. Li, W. Luo, and A. Petropulu, "Toward dual-functional radar-communication systems: Optimal waveform design," *IEEE Trans. Signal Process.*, vol. 66, no. 16, pp. 4264–4279, 2018.
- [7] X. Liu, T. Huang, and Y. Liu, "Transmit Design for Joint MIMO Radar and Multiuser Communications With Transmit Covariance Constraint," *IEEE J. Sel. Areas Commun.*, vol. 40, no. 6, pp. 1932–1950, 2022.
- [8] F. Liu, Y.-F. Liu, A. Li, C. Masouros, and Y. C. Eldar, "Cramér-Rao Bound Optimization for Joint Radar-Communication Beamforming," *IEEE Trans. Signal Process.*, vol. 70, pp. 240–253, 2022.
- [9] L. Chen, F. Liu, W. Wang, and C. Masouros, "Joint radar-communication transmission: A generalized pareto optimization framework," *IEEE Trans. Signal Process.*, vol. 69, pp. 2752–2765, 2021.
- [10] X. Yu, Q. Yang, Z. Xiao, H. Chen, V. Havyarimana, and Z. Han, "A Precoding Approach for Dual-Functional Radar-Communication System With One-Bit DACs," *IEEE J. Sel. Areas Commun.*, vol. 40, no. 6, pp. 1965–1977, 2022.
- [11] N. Levanon and E. Mozeson, *Radar signals*. John Wiley & Sons, 2004.
- [12] M. G. Gaydos, D. J. Love, and T. Kim, "Constant modulus precoded MIMO radar based on Zadoff-Chu sequences," *IEEE Trans. Radar Systems*, pp. 1–1, 2024.
- [13] W. Wu, B. Tang, and X. Wang, "Constant-modulus waveform design for dual-function radar-communication systems in the presence of clutter," *IEEE Aerosp. Electron. Syst. Mag.*, vol. 59, no. 4, pp. 4005–4017, 2023.
- [14] R. Liu, M. Li, Q. Liu, and A. L. Swindlehurst, "Dual-Functional Radar-Communication Waveform Design: A Symbol-Level Precoding Approach," *IEEE J. Sel. Topics Signal Process.*, vol. 15, no. 6, pp. 1316–1331, 2021.
- [15] —, "Joint waveform and filter designs for STAP-SLP-based MIMO-DFRC systems," *IEEE J. Sel. Areas Commun.*, vol. 40, no. 6, pp. 1918–1931, 2022.
- [16] A. Bazzi and M. Chafii, "On integrated sensing and communication waveforms with tunable PAPR," *IEEE Trans. Wireless Commun.*, 2023.
- [17] A. Li, D. Spano, J. Krivochiza, S. Domouchtsidis, C. G. Tsinos, C. Masouros, S. Chatzinotas, Y. Li, B. Vucetic, and B. Ottersten, "A tutorial on interference exploitation via symbol-level precoding: overview, state-of-the-art and future directions," *IEEE Commun. Surveys Tuts.*, vol. 22, no. 2, pp. 796–839, 2020.
- [18] M. Alodeh, S. Chatzinotas, and B. Ottersten, "Constructive multiuser interference in symbol level precoding for the MISO downlink channel," *IEEE Trans. Signal Process.*, vol. 63, no. 9, pp. 2239–2252, 2015.
- [19] A. Li, C. Shen, X. Liao, C. Masouros, and A. L. Swindlehurst, "Practical Interference Exploitation Precoding Without Symbol-by-Symbol Optimization: A Block-Level Approach," *IEEE Trans. Wireless Commun.*, vol. 22, no. 6, pp. 3982–3996, Jun. 2023.
- [20] J. Qian, M. Lops, L. Zheng, X. Wang, and Z. He, "Joint system design for coexistence of MIMO radar and MIMO communication," *IEEE Trans. Signal Process.*, vol. 66, no. 13, pp. 3504–3519, 2018.
- [21] M. F. Keskin, V. Koivunen, and H. Wymeersch, "Limited Feedforward Waveform Design for OFDM Dual-Functional Radar-Communications," *IEEE Trans. Signal Process.*, vol. 69, pp. 2955–2970, 2021.
- [22] X. Liu, T. Huang, N. Shlezinger, Y. Liu, J. Zhou, and Y. C. Eldar, "Joint transmit beamforming for multiuser MIMO communications and MIMO radar," *IEEE Trans. Signal Process.*, vol. 68, pp. 3929–3944, 2020.
- [23] F. Liu, C. Masouros, T. Ratnarajah, and A. Petropulu, "On range sidelobe reduction for dual-functional radar-communication waveforms," *IEEE Wireless Commun. Lett.*, vol. 9, no. 9, pp. 1572–1576, 2020.
- [24] S. H. Dokhanchi, M. R. B. Shankar, M. Alaei-Kerahroodi, and B. Ottersten, "Adaptive Waveform Design for Automotive Joint Radar-Communication Systems," *IEEE Trans. Veh. Technol.*, vol. 70, no. 5, pp. 4273–4290, 2021.
- [25] C. Wen, Y. Huang, L. Zheng, W. Liu, and T. N. Davidson, "Transmit waveform design for dual-function radar-communication systems via hybrid linear-nonlinear precoding," *IEEE Trans. Signal Process.*, 2023.
- [26] X. Yu, X. Yao, J. Yang, L. Zhang, L. Kong, and G. Cui, "Integrated Waveform Design for MIMO Radar and Communication via Spatio-Spectral Modulation," *IEEE Trans. Signal Process.*, vol. 70, pp. 2293–2305, 2022.
- [27] A. J. Duly, D. J. Love, and J. V. Krogmeier, "Time-division beamforming for MIMO radar waveform design," *IEEE Aerosp. Electron. Syst. Mag.*, vol. 49, no. 2, pp. 1210–1223, 2013.
- [28] G. San Antonio, D. R. Fuhrmann, and F. C. Robey, "MIMO radar ambiguity functions," *IEEE J. Sel. Topics Signal Process.*, vol. 1, no. 1, pp. 167–177, 2007.
- [29] A. Li, F. Liu, X. Liao, Y. Shen, and C. Masouros, "Symbol-level precoding made practical for multi-level modulations via block-level rescaling," in *IEEE International Workshop on Signal Processing Advances in Wireless Communications (SPAWC)*, 2021, pp. 71–75.
- [30] G. Hua and S. S. Abeysekera, "Receiver design for range and doppler sidelobe suppression using mimo and phased-array radar," *IEEE Trans. Signal Process.*, vol. 61, no. 6, pp. 1315–1326, 2012.
- [31] X. Yu, K. Alhujaili, G. Cui, and V. Monga, "MIMO radar waveform design in the presence of multiple targets and practical constraints," *IEEE Trans. Signal Process.*, vol. 68, pp. 1974–1989, 2020.
- [32] R. A. Horn and C. R. Johnson, *Matrix analysis*. Cambridge university press, 2012.
- [33] J. Li and P. Stoica, *MIMO radar signal processing*. John Wiley & Sons, 2008.
- [34] B. Lee, A. B. Das, D. J. Love, C. G. Brinton, and J. V. Krogmeier, "Constant modulus waveform design with block-level interference exploitation for DFRC system," *arXiv:2310.10804*, 2023.
- [35] Y.-C. Wang, X. Wang, H. Liu, and Z.-Q. Luo, "On the design of constant modulus probing signals for MIMO radar," *IEEE Trans. Signal Process.*, vol. 60, no. 8, pp. 4432–4438, 2012.
- [36] J. Wang and Y. Wang, "On the Design of Constant Modulus Probing Waveforms With Good Correlation Properties for MIMO Radar via Consensus-ADMM Approach," *IEEE Trans. Signal Process.*, vol. 67, no. 16, pp. 4317–4332, 2019.
- [37] A. Li and C. Masouros, "Interference Exploitation Precoding Made Practical: Optimal Closed-Form Solutions for PSK Modulations," *IEEE Trans. Wireless Commun.*, vol. 17, no. 11, pp. 7661–7676, 2018.
- [38] K. Alhujaili, V. Monga, and M. Rangaswamy, "Transmit MIMO radar beamforming design via optimization on the complex circle manifold," *IEEE Trans. Signal Process.*, vol. 67, no. 13, pp. 3561–3575, 2019.
- [39] J. Yang, A. Li, X. Liao, C. Masouros, and A. Swindlehurst, "Block-level MU-MISO interference exploitation precoding: Optimal structure and explicit duality," *arXiv preprint arXiv:2401.00166*, 2023.
- [40] S. Boyd, N. Parikh, E. Chu, B. Peleato, J. Eckstein *et al.*, "Distributed optimization and statistical learning via the alternating direction method of multipliers," *Foundations and Trends® in Machine Learning*, vol. 3, no. 1, pp. 1–122, 2011.
- [41] Z. Cheng, Z. He, S. Zhang, and J. Li, "Constant modulus waveform design for MIMO radar transmit beampattern," *IEEE Trans. Signal Process.*, vol. 65, no. 18, pp. 4912–4923, 2017.
- [42] X. He and J. Wang, "QCQP with extra constant modulus constraints: Theory and application to sinr constrained mmwave hybrid beamforming," *IEEE Trans. Signal Process.*, vol. 70, pp. 5237–5250, 2022.
- [43] L. Zhao, J. Song, P. Babu, and D. P. Palomar, "A unified framework for low autocorrelation sequence design via majorization-minimization," *IEEE Trans. Signal Process.*, vol. 65, no. 2, pp. 438–453, 2016.
- [44] Y. Li and S. A. Vorobyov, "Fast Algorithms for Designing Unimodular Waveform(s) With Good Correlation Properties," *IEEE Signal Process. Lett.*, vol. 66, no. 5, pp. 1197–1212, 2018.
- [45] Y. Sun, P. Babu, and D. P. Palomar, "Majorization-minimization algorithms in signal processing, communications, and machine learning," *IEEE Trans. Signal Process.*, vol. 65, no. 3, pp. 794–816, 2016.
- [46] J. Song, P. Babu, and D. P. Palomar, "Sequence design to minimize the weighted integrated and peak sidelobe levels," *IEEE Trans. Signal Process.*, vol. 64, no. 8, pp. 2051–2064, 2015.
- [47] L. Xu, J. Li, and P. Stoica, "Radar imaging via adaptive MIMO techniques," in *European Signal Processing Conference*, 2006, pp. 1–5.
- [48] J. Li, P. Stoica, and X. Zheng, "Signal Synthesis and Receiver Design for MIMO Radar Imaging," *IEEE Trans. Signal Process.*, vol. 56, no. 8, pp. 3959–3968, 2008.